Materials & Design 271 (2026) 117112

Contents lists available at ScienceDirect

Materials & Design

journal homepage: www.elsevier.com/locate/matdes

Effect of long-term ageing and associated precipitation on creep deformation behaviour of a Ni based superalloy

Amey Parnaik [a], Vijay Shankar Sridharan [b], Kai Chen [c], G.A. Turichin [d], O.G. Klimova-Korsmik [d], A.H.V. Pavan [e,*], R.L. Narayan [a,*]

[a] Department of Materials Science and Engineering, Indian Institute of Technology, Delhi, Hauz Khas, New Delhi 110016, India
[b] School of Materials Science and Engineering, Nanyang Technological University, 50 Nanyang Avenue, Singapore 639798, Republic of Singapore
[c] Center for Advancing Materials Performance From the Nanoscale (CAMP-Nano), State Key Laboratory for Mechanical Behavior of Materials, Xi'an Jiaotong University, Xi'an 710049, Shaanxi, China
[d] Saint Petersburg State Marine Technical University, Saint Petersburg, Russian Federation
[e] Metallurgy, Materials and Composites Department, Corporate R&D Division, Bharat Heavy Electricals Limited, Vikasnagar 500042, Hyderabad, India

ARTICLE INFO

Keywords:
Creep
γ' shearing
Orowan looping
Deformation mechanisms

ABSTRACT

Creep behaviour of solution-treated and isothermally aged Ni-based superalloy Haynes 282 was investigated in the temperature and stress range of 750–800 °C and 300–420 MPa, respectively. Ageing was carried out at 750 °C for 46, 470, and 6000 h, resulting in progressive γ' precipitate coarsening with negligible grain growth. Creep deformation occurred predominantly in the steady-state and tertiary regimes. The minimum creep rate, $\dot{\varepsilon}_{min}$, initially decreased with ageing and reached its lowest value for the 470 h aged alloy, followed by a marked increase after 6000 h ageing, while rupture life exhibited the opposite trend. The threshold stress corrected-stress exponent, n_{eff}, of all alloys is between 4–7, indicating that the steady-state creep rate is governed by dislocation glide mediated climb. Post-creep microstructural analysis revealed precipitate shearing and stacking faults within γ' precipitates in all samples except the 6000 h aged condition, where γ' precipitates exhibited nanotwins and were surrounded by dense dislocation networks. Variations in creep response are explained by changes in stress required for precipitate shearing or bypass and increasing contribution of dislocation climb in coarser precipitates. Tertiary creep mechanisms leading to intergranular fracture are discussed in brief, and a critical appraisal of service life extrapolation methods is provided.

1. Introduction

Haynes 282, a polycrystalline Ni-based superalloy, is considered as a strong candidate for developing turbomachinery components in gas turbine engines and advanced ultra-supercritical (AUSC) thermal power plants owing to their excellent creep strength, fracture toughness, oxidation resistance, and fatigue strength [1–4]. Since turbomachinery components operate at 700–750 °C for long durations, the most decisive factor that determines the utility of the alloy is its creep strength [5,6]. Considering that the average service life of a component in AUSC power plants is 11 years (or 100,000 h), prior studies have evaluated the creep strength of Haynes 282 by extrapolating the short to medium-term stress rupture test data to 100,000 h [7]. In these stress rupture tests, peak-aged alloys are held at stresses that are higher than the service stress at different temperatures until failure [5,6]. Thereafter, the rupture stress at each temperature is extrapolated for a service life (or rupture time) or 100,000 h. From this, the minimum stress that an alloy can withstand for 100,000 h at 700–750 °C is obtained. Alternately, in some studies, stress rupture testing is performed on peak aged Haynes 282 at different stresses and temperatures for relatively short durations [5,6,8]. Thereafter, using the Larson-Miller Parameter (LMP) approach, where the temperature and rupture time are represented as a single parameter, the maximum permissible service stress for a service duration of 100,000 h and service temperature of 700–750 °C is determined.

In both these extrapolation-based methods, it is assumed that only one creep mechanism is operative throughout the life of the component. This assumption ignores the influence of long-term microstructure evolution on creep behavior [9]. This is particularly concerning in Haynes 282 as its primary high and room temperature strengthening phase, γ', progressively undergoes coarsening at the designated service

* Corresponding authors.
E-mail addresses: pavanahv@bhel.in (A.H.V. Pavan), rlnarayan@iitd.ac.in (R.L. Narayan).

https://doi.org/10.1016/j.matdes.2026.117112
Received 20 June 2026; Received in revised form 29 August 2026; Accepted 21 September 2026
Available online 22 September 2026
0264-1275/© 2026 The Authors. Published by Elsevier Ltd. This is an open access article under the CC BY license (http://creativecommons.org/licenses/by/4.0/).

temperature. While short-term creep testing captures only marginal changes in the γ' phase, which does not affect the creep mechanisms, significant γ′ coarsening after prolonged service can potentially alter the rate-controlling processes within the dislocation glide–climb controlled creep mechanism. This change in the rate controlling step in creep mechanism, which is not accounted for in extrapolation methodologies, could potentially affect the total creep life. In addition, most studies on Haynes 282 have so far focused on determining the stress exponents and estimating activation energies from short-term creep data [6,8,10,11]. While these are useful for understanding the creep mechanisms, they do not provide the entire gamut of information on mechanisms leading to creep failure.

Recognizing the importance of long-term microstructural evolution on the mechanical properties of Haynes 282, our recent studies investigated the effect of isothermal ageing on its high- and room-temperature tensile properties, impact properties [4], and room-temperature fatigue behaviour [12,13]. The aging conditions in these studies were selected using an accelerated aging (AA) methodology, which uses the Larson Miller Parameter (LMP) to represent long-term service exposure at 700 °C for 100,000 h [4]. Based on this approach, ageing treatments of 6000 h at 750 °C, 470 h at 800 °C, and 46 h at 850 °C were identified as conditions representative of long-term service exposure. These studies showed that, although the high- and room-temperature yield and tensile strengths remained comparable across the aged conditions, significant differences were observed in ductility, impact toughness, and room-temperature fatigue strength [4,12,13]. These differences demonstrated that ageing-induced microstructural evolution can substantially influence the mechanical performance of Haynes 282, even when conventional strength parameters remain relatively unchanged.

An important outcome of these studies was the identification of microstructure–property correlations associated with γ′ precipitate coarsening and carbide evolution, including the influence of γ′ size on fatigue strength and the role of carbide networks in ductility and impact toughness [4,12,13]. However, the influence of ageing-induced microstructural changes on the creep behaviour of Haynes 282 has received comparatively limited attention [8,10,14,15]. In particular, the progressive evolution of γ′ precipitates and carbide phases during long-term exposure may alter the deformation and recovery processes governing creep, which is not accounted for in conventional extrapolation approaches based on short-term creep data.

To address this research gap, the creep behaviour of solution-treated and isothermally aged Haynes 282 was investigated at temperatures and stresses in the range of 750–800 °C and 300–420 MPa, respectively. For this purpose, the alloy was isothermally aged at 750 °C for 46, 470, and 6000 h. While the specific ageing durations are motivated by our previous isothermal ageing treatments to supplement the AA strategy, in this study, they represent ageing timescales that are 3 orders of magnitude apart. Results indicate that the minimum creep rate decreases with increasing ageing duration for up to 470 h, but increases significantly, when the ageing time is increased to 6000 h. Alternately, the rupture time follows the opposite trend. Larson-Miller Parameter vs. rupture stress plots confirm that these trends are similar for the range of temperatures used in the study. These results are explained on the basis of subtle changes in the rate controlling step in creep mechanisms owing to the coarsening of γ' precipitates. Finally, a critical appraisal of extrapolation-based approaches to determine the long-term creep behaviour of Haynes 282 from short term tests is provided.

2. Materials and methods

2.1. Materials

A polycrystalline γ'-precipitation strengthened Ni-based superalloy, Haynes 282, is procured from M/s Haynes International, USA, in a hot-rolled and solution-annealed condition at 1050 °C ± 30 °C for 1 h, followed by water quenching. The hot-rolled and solution annealed Haynes 282 is henceforth referred to as the As-Received (AR) sample. The nominal and experimentally measured chemical compositions of Haynes 282, as provided in our previous study [4], are reproduced in Table 1. An isothermal ageing treatment is performed on the AR alloy at 750 °C for ageing duration, t_a of 46, 470, and 6000 h, and corresponding aged conditions are referred to as HT46, HT470, and HT6000, respectively.

2.2. Creep tests

Creep specimens were machined using wire-cut electric discharge machining (EDM) from the AR and aged plates, with a gauge diameter of 7 mm and gauge length of 35 mm (see **Fig. S1**), following the specimen geometry specified in ASTM E8M [17]. The creep tests were conducted in accordance with ASTM E139 [18]. Note that the tensile loading axis is along the rolling direction for the samples extracted from AR and aged plates. Creep tests are performed at temperatures of 750 °C, 775 °C, and 800 °C with rupture stress values ranging from 300 MPa to 420 MPa. Note that the range of chosen creep stresses is significantly higher than the service stress of 100–200 MPa. However, this choice is driven by the condition that the creep rupture time (t_r) is $<$ 2000 h, which is the typical limit for acceptable lab-scale creep testing duration [8,18]. During the creep tests, the strain is measured using a clip-on extensometer assembly clamped to both ends of the gauge length. This assembly extends as the test progresses and the sample deforms. The deformation is then translated to the extension of the connecting plates at the exterior of the furnace, to which a dial gauge is attached at one end, and a blank plate is present at the other. This dial gauge subsequently reads the extension between the connecting plates as a function of test duration.

2.3. Microstructural characterization

AR and aged samples, both before and after creep deformation, are subjected to detailed microstructural characterization. For metallographic investigations, a sequential grinding process is employed, using emery papers with grit sizes ranging from #300 to #4000, followed by cloth polishing with a 50 nm colloidal silica suspension. Subsequently, the specimens are etched using Kallings No. 2 reagent, which consists of 1-gram $CuCl_2$, 20 ml HCl, and 20 ml ethanol. Undeformed samples are sectioned to obtain back-scattered electron (BSE) images along the normal direction using a JEOL JSM-7800F Prime Field Emission Scanning Electron Microscope (FESEM), which is also equipped with Electron Backscattered Diffraction (EBSD) and Energy Dispersive Spectroscopy (EDS) detectors. Additionally, EBSD maps are also obtained on the same plane for detailed analysis of grain morphology. X-ray diffraction is performed on AR and aged samples using a Rigaku Ultima IV multipurpose X-ray diffractometer to identify different phases. Scans were performed in the angular range of 30° to 100° with a step size of 0.01° s^{-1} using Cu K_α radiation. The diffractograms obtained were further processed and analyzed using the X-pert High Score Plus software. For HRTEM investigation of creep-deformed samples, thin foils are extracted from the uniformly deformed gauge section, located at least 15 mm from the fractured surface. These foils are subjected to electrolytic thinning in a solution containing 10 % perchloric acid and 90 % ethanol at −25 °C. For metallographic examination of creep-tested samples, the AR and aged samples tested at 750 °C and 300 MPa are selected, as they have the highest t_r. A JEOL JEM-ARM200F NEOARM High-Resolution Transmission Electron Microscopy (HRTEM) equipped with a cold Field Emission Gun (FEG) operating at 200 kV is utilized for a detailed investigation of dislocation substructure, their interaction with different microstructural features, and characterization of second-phase particles. Fractography is also performed on the same AR and aged creep-tested samples using FESEM.

Table 1
Chemical composition of Haynes 282 [4].

Chemical composition	Cr	Co	Mo	Ti	Al	Fe	Mn	Si	C	B	Ni
Nominal [16]	20	10	8.5	2.1	1.5	1.5 max.	0.3 max.	0.15 max.	0.06	0.005	Bal.
Actual	18.7	9.7	8.8	2.2	1.5	0.8	0.03	0.07	0.05	0.004	Bal.

3. Results

3.1. Microstructural characterization of AR and aged Haynes 282

Fig. 1 shows the low and high-magnification backscattered electron (BSE) images of AR and aged samples. AR sample has 90 ± 8 μm sized equiaxed grains. In addition, there are several small and large precipitates within the grains and at the grain boundaries. The sizes of these precipitates are measured and listed in Table 2. The large precipitates have an average size of 4.5 ± 1.8 μm, whereas the small precipitates, which have a brighter contrast, have an average size of 0.35 ± 0.1 μm. Based on our previous work, these precipitates are identified as Ti/Mo-rich MC carbides and Mo-rich M_6C carbides, respectively [4,12,13]. Note that $M_{23}C_6$ carbides and γ' precipitates are absent in the AR sample as the solution annealing treatment is performed at 1050 °C, which is higher than their solvus temperatures [1,19]. From the inverse pole

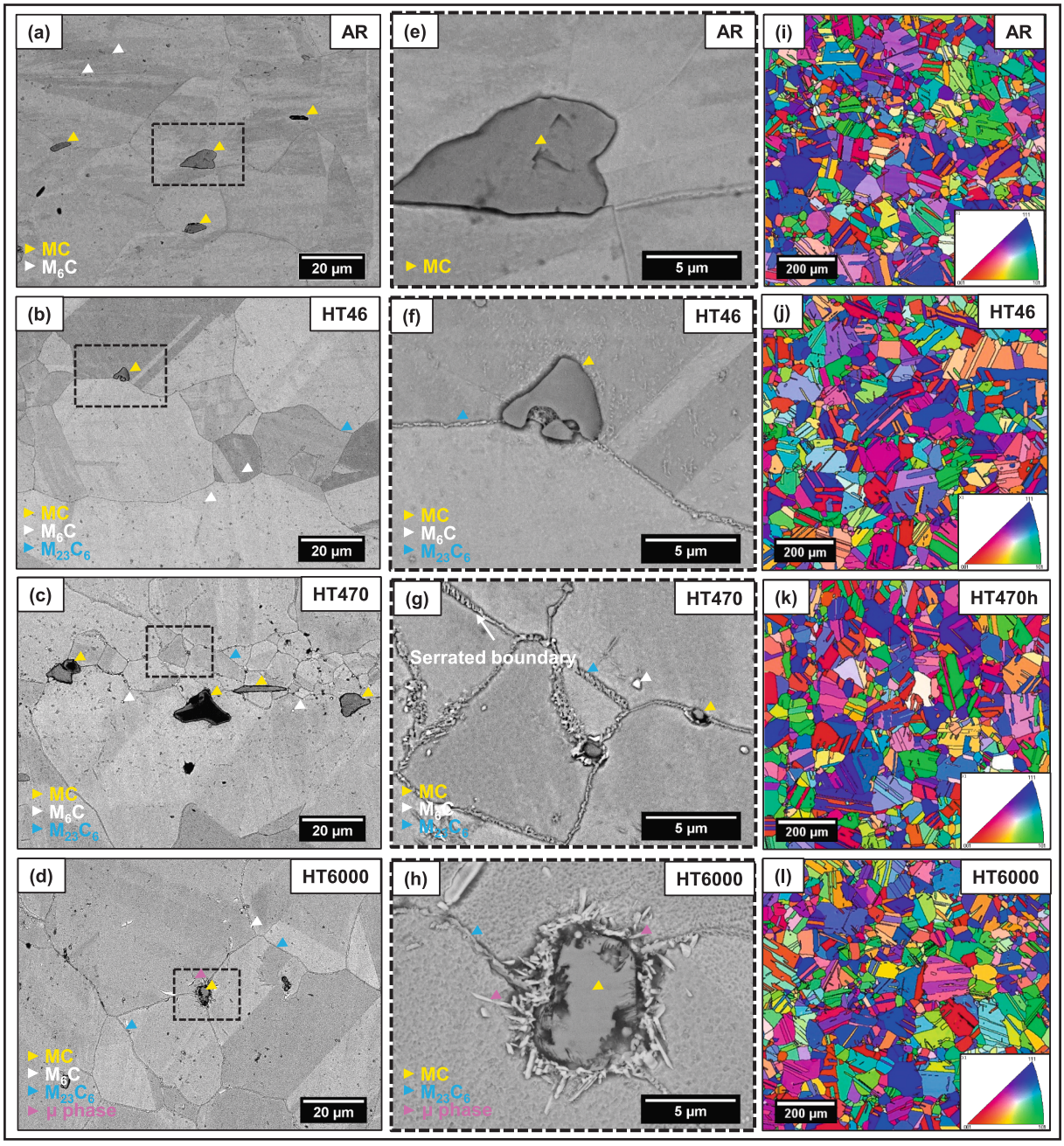


Fig. 1. Representative BSE images of (a) AR, (b) HT46, (c) HT470, and (d) HT6000 samples. (e) to (h) are corresponding high-magnification images of AR, HT46, and HT470 and HT 6000 samples, respectively. IPF maps of (i) AR, (j) HT46, (k) HT470, and (l) HT6000 samples.

Table 2
Microstructural features observed in undeformed AR and aged samples.

Condition	Average grain size (μm) [4]	*d*(nm) [4]	λ (nm)	δ (%)	Average MC carbide size (μm)	Average M_6C carbide size (μm)	Fraction of twin boundary length
AR	90 ± 8	–	–	–	4.5 ± 1.8	0.4 ± 0.1	0.58
HT46	107 ± 21	20 ± 4	27 ± 6	−0.058	5.8 ± 1.5	0.5 ± 0.2	0.63
HT470	114 ± 21	44	55	−0.067	5.7 ± 3.0	0.7 ± 0.3	0.60
HT6000	163 ± 48	120 ± 27	165 ± 37	−0.174	4.0 ± 1.1	0.5 ± 0.2	0.59

figure (IPF) maps, shown in Fig. 1i, it is evident that the AR sample has a random texture and a significant number of annealing twins. The area fraction of the twin boundaries is measured and listed in Table 2**.** Note that the area fraction of twin boundaries in the AR sample is ~ 58 % (see Fig. 1i).

Fig. 1b-h show the low and high-magnification SEM images of the HT46, HT470, and HT6000 samples. Much like that seen in the AR sample, the grains of HT46, HT470, and HT6000 samples are also equiaxed and contain fine and coarse precipitates within them. The average grain size of the HT46 and HT470 samples are 107 ± 21 μm and 114 ± 21 μm, respectively, whereas in the HT6000 sample, the grain size is 163 ± 48 μm, which is 50 % larger. However, considering the significant ageing time of the sample, the grain growth can be considered relatively limited. Interestingly, the size of MC and M_6C precipitates in HT46 sample is 5.8 ± 1.5 μm and 0.5 ± 0.2 μm, respectively, which is similar to that in the AR sample. Moreover, the average sizes of MC and M_6C precipitates in HT470 and HT6000 samples are also similar to those in the AR sample (refer to Table 2). However, at the grain boundaries of these samples, Cr-rich $M_{23}C_6$ carbides (labelled with blue arrows) are observed. In addition, the $M_{23}C_6$ carbides form a continuous network along the grain boundaries of all samples.

Besides these carbides, all the aged samples contain fine γ' precipitates. In our previous study [4,12,13], these precipitates were characterized via TEM. The area fraction of γ' precipitates in all samples is 20 %, which matches well with that obtained from the simulated phase diagram of Haynes 282 (see **Fig. S2**). In our previous work [4,12], the size of these spherical precipitates, *d*, and their interparticle spacings, λ, was measured, which is listed in Table 2. In HT46 and HT470 samples, the γ' size is ~20 ± 4 and ~44 nm, respectively, whereas that in the HT6000 sample is 120 ± 27 nm, which is significantly coarser. The corresponding λ measured for HT46 and HT470 samples are 27 ± 6 and 55 nm, respectively. However, for the HT6000 sample, λ is 165 ± 37 nm, which is significantly higher than those of the HT46 and HT470 samples.

In addition, note that the Mo-rich M_6C carbides in HT46 and HT470 samples form at the MC/γ interfaces. These M_6C carbides (indicated by white arrows in Fig. 1g) appear bright in BSE images due to the higher atomic number of Mo. However, in the HT6000 sample, the topologically close-packed (TCP) μ phase, $(Ni, Co, Fe)_7Mo_6$, with a hexagonal crystal structure, is observed to form at the MC/γ-matrix interface, as indicated by the pink arrows in Fig. 1h and S3. These μ- phase exhibit needle-like morphology, are brittle in nature, and often act as a site for crack nucleation [20].

Fig. 2 shows the XRD scans of AR, HT46, HT470, and HT6000 samples. Peaks corresponding to the (111), (200), (220), (311), and (222) planes of the face-centred cubic (FCC) γ phase are observed in all the samples. However, no peaks corresponding to $M_{23}C_6$, M_6C, and MC phases are observed in the scans. This is the outcome of the fact that the volume fraction of the carbide phases is lower than the detection limit of XRD. It is also observed that the peaks of γ and γ' phases, owing to their similar lattice parameters, overlap. Average lattice parameters of γ, a_γ, and γ', $a_{\gamma'}$ are calculated by deconvoluting each unsymmetric peak in the XRD scan. The representative deconvoluted (200) peaks of γ and γ' phases in the HT46, HT470, and HT6000 samples are shown in Fig. 2b-d. Note that the integrated intensity (area) of the XRD peaks corresponding to the γ and γ′ phases are in a ratio of 1/5, which reflects the relative volume fractions of these phases present in the alloy. The lattice misfit, δ, between the γ and γ' phases is estimated using [21],

$$\delta = \frac{2(a_{\gamma'} - a_\gamma)}{(a_\gamma + a_{\gamma'})} \quad (1)$$

Estimated δ values are listed in Table 2**.** δ of HT46 and HT470 samples

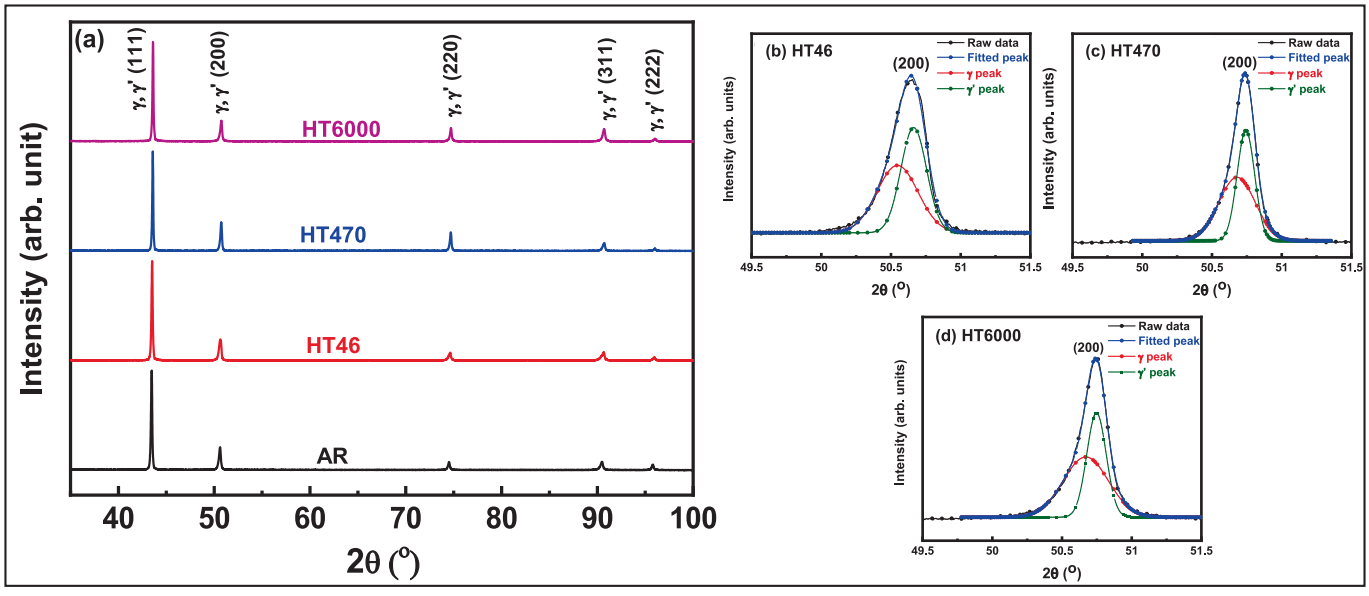


Fig. 2. (a) X-ray diffraction patterns of AR and aged samples. Deconvoluted (200) peak of (b) HT46, (c) HT470, and (d) HT6000 samples.

are −0.058 % and −0.067 %, respectively, whereas that of HT6000 is −0.174 %, which is significantly higher.

Overall, ageing of the AR sample leads to several microstructural changes. While increasing ageing time leads to limited but some grain growth, it leads to the formation of $M_{23}C_6$ carbides at grain boundaries. Moreover, ageing leads to the reduction in the size of MC carbides and the evolution of M_6C precipitates at the MC/γ interfaces. At significantly longer ageing durations, these M_6C precipitates transform to the TCP-μ phases. Ageing also leads to the nucleation of γ' precipitates, which coarsen and their lattice misfit increases with increasing ageing duration.

3.2. Creep behaviour of AR and aged samples

Creep strain, ε vs. time, *t*, plots for AR, HT46, HT470 and HT6000 samples at different rupture stress, σ_r, and testing temperatures, *T*, are shown in **Fig. S4**. In all plots, ε increases non-linearly with increasing *t*. The rupture strain (ε_r), time to rupture (t_r), and the percentage of creep life spent in the primary, secondary, and tertiary regimes were determined from the creep strain–time curves. The minimum creep rate was estimated from the creep rate–time curves. The corresponding values for all samples are listed in **Table S1**. In all the samples, except HT6000, there is no discernible primary creep regime. In the HT6000 samples, a discernible but limited primary creep regime is observed, which varies from 0 to 5 % of the total creep life (see **Fig. S4d** and **Table S1**).

In the AR sample, the % life in secondary creep regime is in the range of 26.3–38.5 %. However, in the HT46 sample, the range of % life in the secondary regime is 21.4–43.9 %, which is slightly broader. For the HT470 and HT6000 samples, the range of % life in secondary regime is 33–45.3 % and 47.5–54.3 %, respectively. Overall, the average % life spent in the secondary regime for AR, HT46, and HT470 is 32 %, 36 %, and 38 %, respectively. However, % life spent in the secondary regime of the HT6000 sample is 50 %, which is significantly higher. In contrast, in the AR, HT46, and HT470 samples, ≥50 % life is spent in the tertiary creep regime (see **Table S1**). The range of % life in the HT6000 sample spent in the tertiary regime is 41.3–51.5 %, which is also significant but slightly lower than that of other samples.

Fig. 3a displays rupture stress, σ_r vs. rupture time, t_r plots of AR and aged samples. At $T = 750$ °C and $\sigma_r = 300$ MPa, the t_r of AR, HT46, and HT470 samples are 1253 h, 1413 h, and 1746 h, respectively. However, in HT6000, t_r reduces to 1083 h, which is even lower than the t_r of AR sample. The increase in t_r in HT46 and HT470 samples compared to AR sample and its decrease in HT6000 sample is consistently observed in samples tested at $T = 750$ °C and $\sigma_r = 360$, 390, and 420 MPa. Moreover, a similar trend is evident when AR, HT46, HT470, and HT6000 samples are tested at a constant $\sigma_r = 390$ MPa, but with varying $T = 750$ °C to 800 °C, as shown in Fig. 3b. Furthermore, it is noted that at $T = 750$ °C and $\sigma_r > 390$ MPa, the difference in t_r between HT6000 and the other samples increases drastically (see Fig. 3a). For instance, at $\sigma_r = 420$ MPa, the t_r of the HT6000 sample is only 59 h, which is about 50 % of that of the AR sample. In contrast, at $\sigma_r = 300$ MPa, the reduction in t_r for HT6000 compared to the AR sample is only 14 %.

Fig. S5 shows the evolution of creep rate, $\dot{\varepsilon}$ with *t* for AR, HT46, HT470 and HT6000 samples. Across all the investigated samples, the $\dot{\varepsilon}$ initially decreases until reaching a minimum value, which is referred to as the minimum or steady-state creep rate, $\dot{\varepsilon}_{min}$. This is followed by a steep increase in $\dot{\varepsilon}$ in the tertiary stage before failure. The $\dot{\varepsilon}_{min}$ of AR and aged samples are listed in **Table S1**. Note that, for AR, HT46, HT470, and HT6000 samples, the decline in creep rate prior to reaching $\dot{\varepsilon}_{min}$ is relatively small, which validates the previous assertion regarding the presence of a limited primary creep regime (see **Table S1**). Furthermore, $\dot{\varepsilon}_{min}$ consistently increases with an increase in σ_r or *T*. Note that for any combination of *T* and σ_r, $\dot{\varepsilon}_{min}$ is similar in the AR, HT46 and HT470 samples. Moreover, $\dot{\varepsilon}_{min}$ of HT6000 is significantly higher. For example, at $\sigma_r = 300$ MPa and $T = 750$ °C, the $\dot{\varepsilon}_{min}$ of AR, HT46 and HT470 samples are in the range of ~ 1.7–2.3 x 10^{-9} s^{-1}. In contrast, the HT6000 sample has an order of magnitude higher $\dot{\varepsilon}_{min}$ of ~ 1.6 x 10^{-8} s^{-1}. The same is observed for tests performed at $T = 750$ °C and $\sigma_r = 360$, 390, and 420 MPa.

Fig. 4a shows the plot of $\dot{\varepsilon}_{min}$ vs. σ_r for all the samples. The steady-state creep behavior of Ni-based superalloys under constant stress and temperature is well described by Norton-Arrhenius creep law [22], which is,

$$\dot{\varepsilon}_{min} = A\sigma_r^n exp\left(\frac{-Q_{app}}{RT}\right) \quad (2)$$

where *A* is the material and temperature-dependent constant, *n* is the stress exponent, which signifies the rate-controlling steady-state creep mechanism, Q_{app} is the apparent activation energy for creep, and *R* is the universal gas constant. Q_{app} is estimated from the slope of $\ln(\dot{\varepsilon}_{min})$ vs. $(1/T)$ plot, shown in Fig. 4b, at $\sigma_r = 390$ MPa. For the AR and HT6000 samples Q_{app} is 290 and 283 kJ/mol, respectively, which are similar to the reported activation energy for self-diffusion of Ni, which is in the range of 280–300 kJ/mol [23]. In contrast, Q_{app} of HT46 and HT470 are 444 kJ/mol and 470 kJ/mol, respectively, which are significantly higher.

Furthermore, *n* values obtained for AR and aged samples are in the range of 7–10 (see Fig. 4a), which is significantly higher than that observed in the power law creep regime, where *n* should be in the range of 3–7. This suggests that the threshold stress, σ_{th}, formulation can be applied to interpret the creep deformation behavior of Haynes 282, with σ_{th} representing an effective stress below which the contribution to creep deformation is negligible. The σ_{th} is estimated by plotting $\dot{\varepsilon}_{min}^{(1/neff)}$ versus σ_r and performing a linear fit. The fitted line is then extrapolated to a point on the x-axis where $\dot{\varepsilon}_{min}^{(1/neff)} = 0$ (see Fig. 5a). Note that σ_{th} in AR and HT46 samples are 59 and 96 MPa, respectively. Moreover, in HT470 and HT6000 samples, σ_{th} is 154 and 183 MPa, respectively. Subtracting the contribution of σ_{th} from σ_r, the effective rupture stress, σ_{eff} is estimated. The plot of $\dot{\varepsilon}_{min}$ vs. σ_{eff} is shown in Fig. 5b. The effective stress exponent, n_{eff}, estimated from slope of $\dot{\varepsilon}_{min}$ vs. σ_{eff} plot are in the range of 4.7–5.9, indicating that creep recovery is dominated by a dislocation-climb-controlled mechanism in all samples.

The σ_r vs. Larson-Miller Parameter (LMP) plots are shown in Fig. 6a. LMP for each σ_r is calculated from [9],

$$LMP = T[\log(t_r) + C] \quad (3)$$

where *T* is the creep temperature in Kelvin (K), t_r is the rupture time in hours (h), and $C = 20$ is the LMP constant for Haynes 282 [24]. Using these plots, the permissible stress of service of AR, HT46, HT470, and HT6000 samples for the expected service life and service temperature can be calculated. For the service conditions of 700 °C for 100,000 h of creep, where the latter is equated with $t_r \sim 10^5$h, LMP is 24325. Therefore, σ_r of AR and HT46 are 223 and 228 MPa, respectively. However, HT470 has the highest σ_r of 239 MPa while that of HT6000 is 218 MPa, which is the lowest. Regardless, for the service duration of 100,000 h at 700 °C, σ_r in all samples is higher than the service stress of 100 MPa [16]. This suggests that a factor of safety of 2.2–2.4 is sufficient for designing components using Haynes 282.

Additionally, for a specified service temperature and stress, LMP directly scales with t_r. Therefore, from the LMP plots it is evident that for the entire range of temperature and σ_r, HT6000 and HT470 have the lowest and highest t_r. While HT46 has higher t_r than that of AR, they are similar at $\sigma_r > 390$ MPa. It is also noteworthy that for $\sigma_r > 390$ MPa, t_r of HT6000 starts dramatically decreasing compared to other samples.

The variations of $\dot{\varepsilon}_{min}$ as a function of t_r for AR and aged samples is shown in the Fig. 6b. These plots indicate that the creep data of all alloys follow a simple Monkman-Grant relationship [25], which is,

$$\dot{\varepsilon}_{min} t_R = C_{MG} \quad (4)$$

The product of $\dot{\varepsilon}_{min}$ and t_r is Monkman-Grant constant (C_{MG}). C_{MG} also

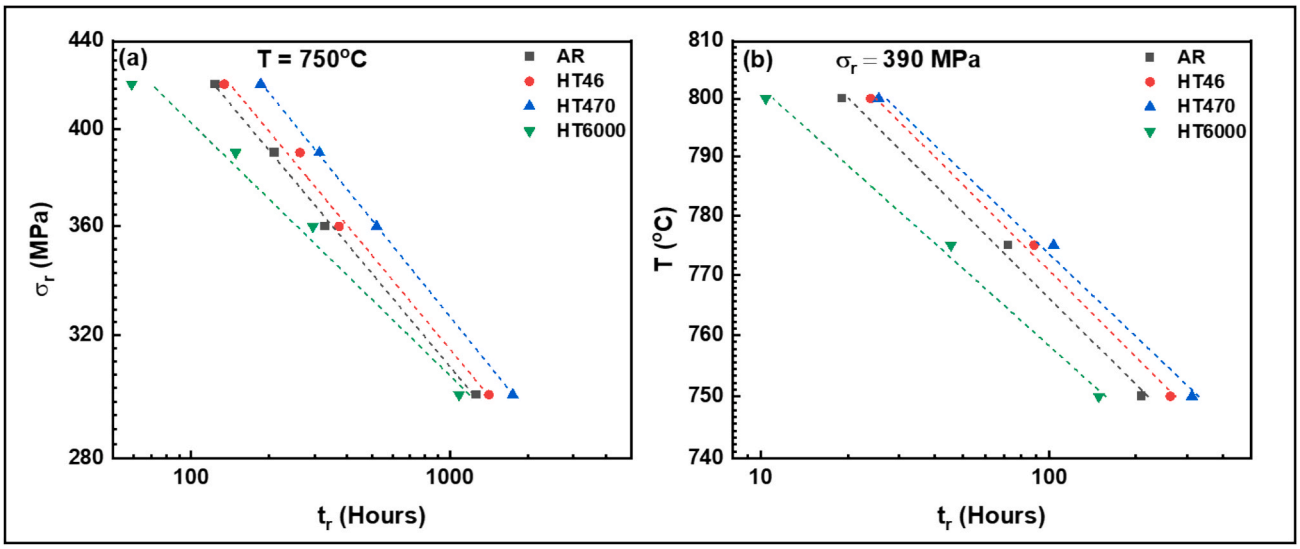


Fig. 3. (a) Variations of creep rupture time (t_r) as a function of rupture stress (σ_r) for AR and aged samples at 750 °C. (b) Dependence of rupture time (t_r) on creep test temperature (T).

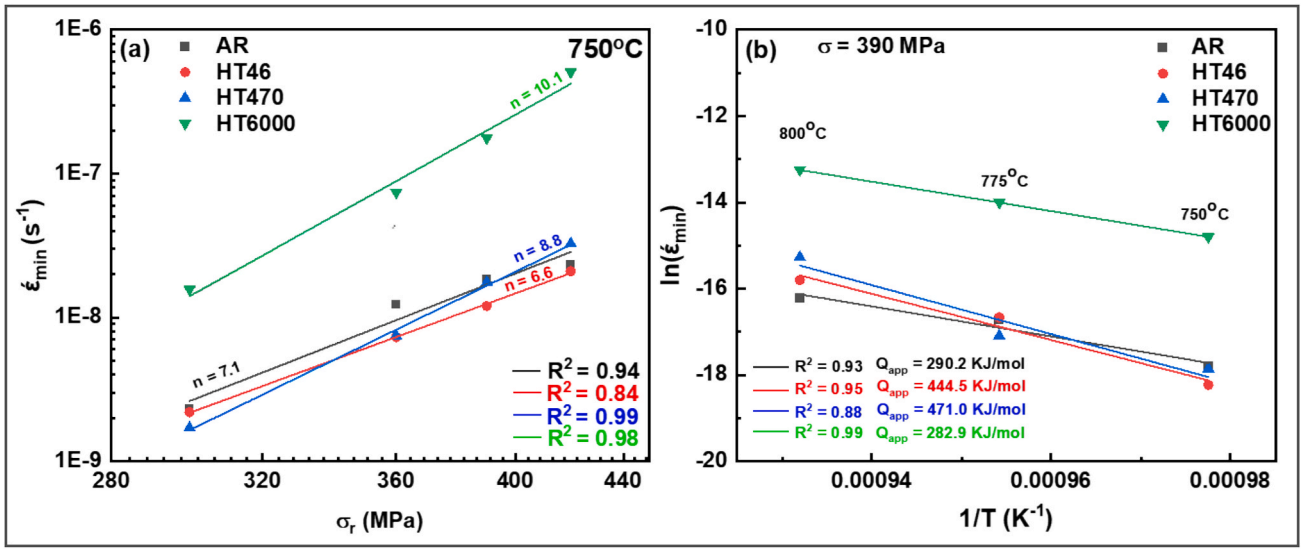


Fig. 4. Variations of (a) minimum creep rate ($\dot{\varepsilon}_{min}$) vs. rupture stress (σ_r) (b) Plot of ln ($\dot{\varepsilon}_{min}$) vs. 1/T for AR and aged samples.

provides a rough measure of the $\dot{\varepsilon}$ in the steady state regime, provided the primary creep life is insignificant. While C_{MG} of AR, HT46 and HT470 are similar and in the range of ~0.011–0.017, that of HT6000 is ~0.088, which is significantly higher. Moreover, from these plots, the $\dot{\varepsilon}_{min}$ at the service condition of 700 °C for 100,000 h can be calculated for all samples. Equating the service life to $t_r \sim 10^5$h, $\dot{\varepsilon}_{min}$ of AR, HT46, HT470 are 3.14×10^{-11} s^{-1}, 3.56×10^{-11} s^{-1}, 4.61×10^{-11} s^{-1}, which are within the same order of magnitude, whereas that of HT6000 is 2.44×10^{-10} s^{-1}, which is much higher.

Overall, ageing of the solution treated sample results in an increase in creep rupture life with aging duration up to 470 h. However, prolonged aging to 6000 h leads to a reduction in creep life compared to the AR sample. Furthermore, σ_{th} increases with ageing duration. The estimated true-stress exponents of all alloys are in the range of 4.7–5.9, which implies that steady-state creep is dominated by a dislocation-climb-controlled mechanism in all samples.

3.3. Microstructural evolution of creep-deformed AR and aged samples

Fig. 7 shows BSE images of creep-tested AR, HT46, HT470, and HT6000 samples tested at $T = 750$ °C and $\sigma_r = 300$ MPa. Fig. 7a shows the microstructure of a creep-tested AR sample. The average grain size of the creep-tested AR sample is 123 ± 14 μm, which is slightly higher than 90 ± 8 μm in the undeformed sample. In addition, Mo-rich M_6C carbides are observed at the MC/γ-matrix interface, highlighted by white arrows in Fig. 7a. These carbides appear brighter in the Z-contrast BSE image. The average size of MC carbides in the creep-tested AR sample is 3.5 ± 2.0 μm, which is slightly smaller than its undeformed counterpart, whereas M_6C carbides with a size of 0.6 ± 0.2 μm are slightly coarser than their undeformed counterparts (refer to Table 3). Moreover, a semi-continuous network of Cr-rich $M_{23}C_6$ carbides is observed along the grain boundaries, as highlighted by blue arrows. Within this grain boundary carbide network, small brighter regions also indicate localized M_6C precipitation.

Fig. 7b, c, and d show the BSE images of creep-tested HT46, HT470, and HT6000 samples respectively, which are tested at $T = 750$ °C and σ_r

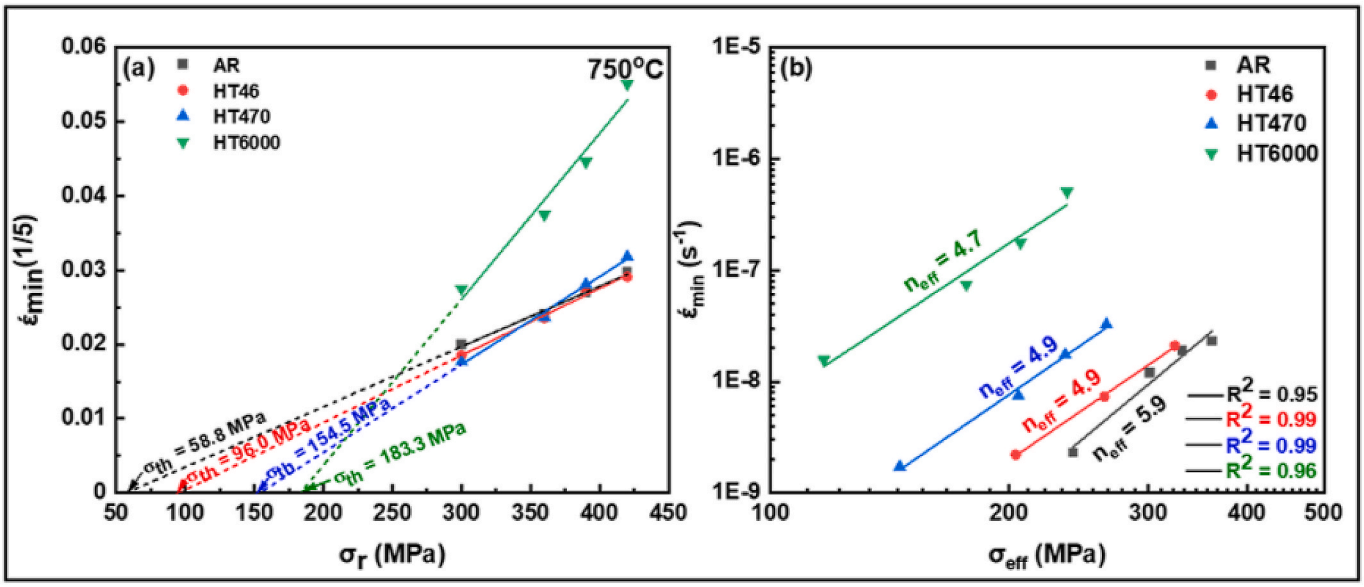


Fig. 5. (a) Minimum creep rate $(\dot{\varepsilon}_{min})^{(1/n)}$ vs. rupture stress (σ_r) for determination of threshold stress (σ_{th}) values of AR and aged samples, (b) Minimum strain rate $(\dot{\varepsilon}_{min})$ vs. effective rupture stress (σ_{eff}) for the determination of effective stress exponents (n_{eff}) of AR and aged samples.

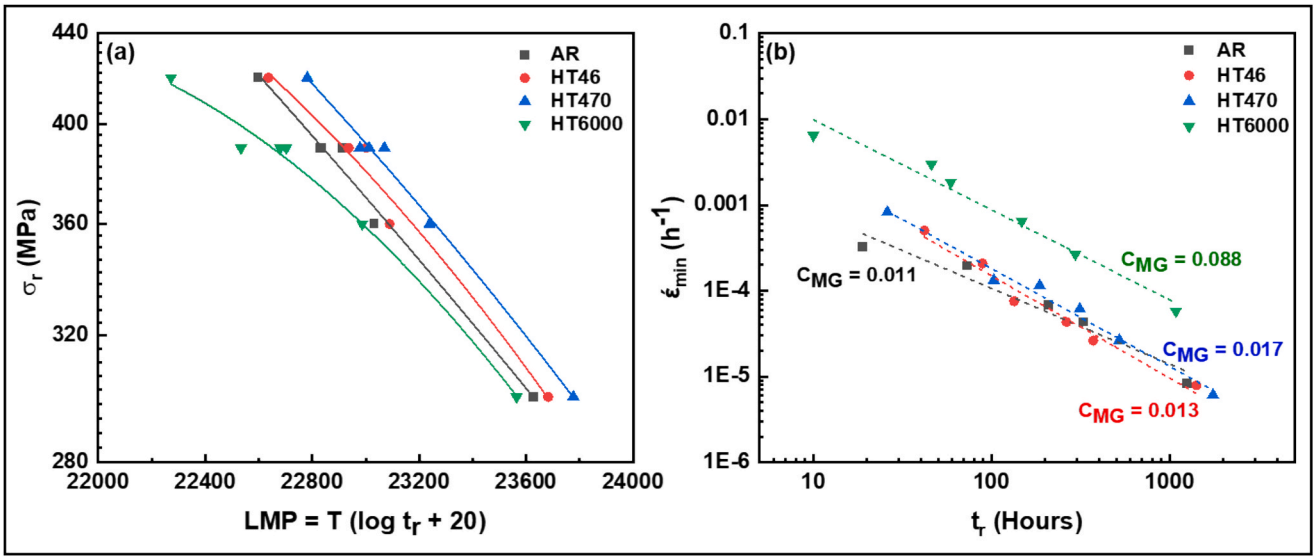


Fig. 6. Variations of (a) rupture stress (σ_r) vs. LMP (b) Minimum creep rate $(\dot{\varepsilon}_{min})$ vs. rupture time (t_r).

= 300 MPa. Average grain sizes of creep-tested HT46, HT470, and HT6000 creep-tested samples are 112 ± 17, 118 ± 18, and 170 ± 42 μm, respectively, which are similar to their corresponding undeformed counterparts. The grain boundary carbide network is denser and more continuous after creep rupture in all three samples. Bright regions within the grain boundary carbide network appear more frequently, indicating increased precipitation of Mo-rich M_6C carbides during creep exposure. Similar to the AR sample, the average size of MC and M_6C carbides in the creep-tested HT46 sample is 4.6 ± 1.0 and 0.9 ± 0.3 μm, respectively, which are slightly finer and coarser, respectively, compared to their undeformed counterparts (see Table 3). Similarly in HT470 and HT6000 sample MC carbides are slightly finer and M_6C carbides are slightly coarser compared to their undeformed samples. A similar trend was observed in the HT470 and HT6000 sample (see Table 3). Moreover, the creep-tested HT6000 sample also contains the Mo-rich needle-shaped TCP-μ phase that was observed in its pre-creep testing counterpart.

The γ' precipitate sizes and resulting submicroscopic deformation modes during creep are systematically investigated using high-resolution transmission electron microscopy (HRTEM) for all creep-tested samples tested at T = 750 °C and σ_r = 300 MPa, as shown in Figs. 8-9. The TEM images of the creep-tested AR sample are shown in Fig. 8. Fig. 8a shows a High-Angle Annular Dark Field (HAADF) Scanning Transmission Electron Microscopy (STEM) image, obtained along [011] zone axis, which reveals uniformly distributed spherical γ' precipitates within the γ matrix. The corresponding EDS elemental map shown in Fig. 8a1 confirms that γ' precipitates are enriched in Al, Ti, and Ni, and hence corresponds to Ni_3 (Ti, Al) phase with $L1_2$ crystal structure [26]. In Table 3, d and λ of γ' precipitates in AR sample are listed. They are 60 ± 15 nm and 83 ± 21 nm, respectively. Note that prior to creep testing, AR sample is devoid of γ' precipitates, suggesting that γ' precipitation occurs during creep exposure at T = 750 °C for t_r = 1253 h. Additionally, Fig. 8b shows the lattice fringes of the γ matrix and the γ' precipitate. The corresponding Fast Fourier Transform (FFT) obtained from green and blue dashed regions is shown in Fig. 8b1 and 8b2,

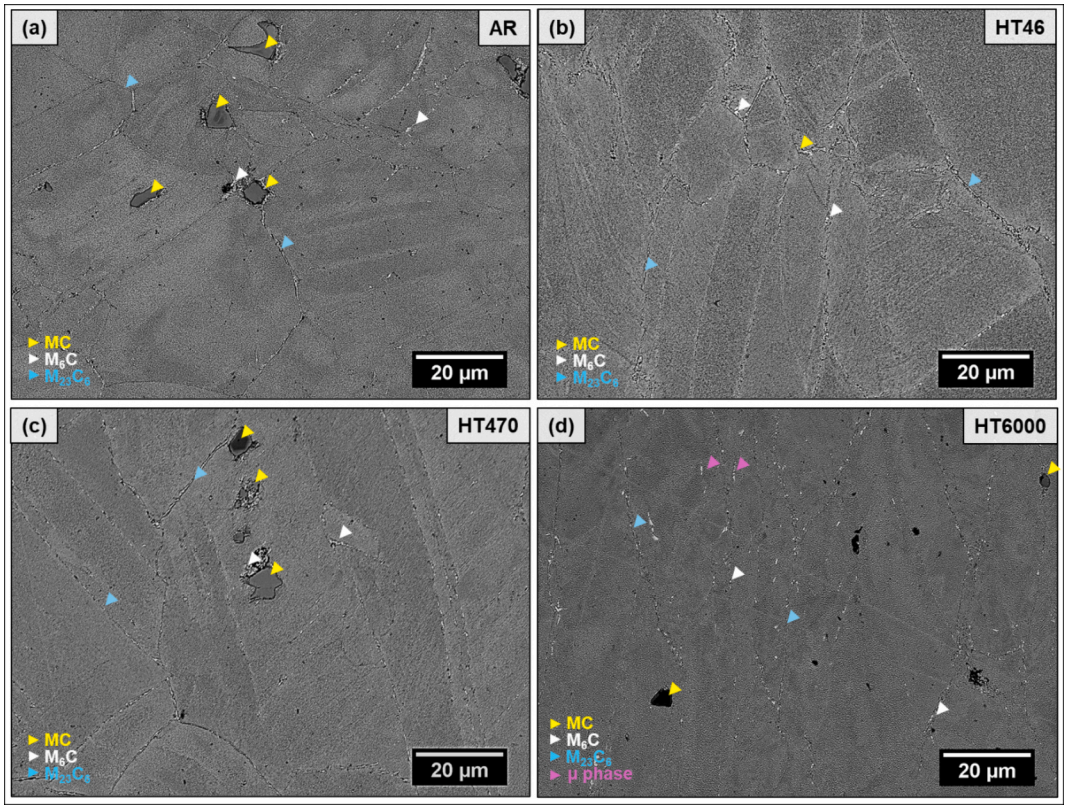


Fig. 7. Representative BSE images of creep-tested samples tested at $T = 750$ °C and $\sigma_r = 300$ MPa for (a) AR (b) HT46, (c) HT470, and (d) HT6000.

Table 3
Microstructural features observed in creep-tested AR and aged samples.

Condition	Average grain size (μm)	d (nm)	λ (nm)	δ (%)	Average MC carbide size (μm)	Average M_6C carbide size (μm)
AR	123 ± 14	60 ± 15	83 ± 21	−0.191	3.5 ± 2.0	0.6 ± 0.2
HT46	112 ± 17	73 ± 13	101 ± 18	−0.234	4.6 ± 1.0	0.9 ± 0.3
HT470	118 ± 18	90 ± 17	124 ± 23	−0.312	3.2 ± 1.0	1.1 ± 0.2
HT6000	170 ± 42	137 ± 27	189 ± 37	−0.391	2.5 ± 0.8	0.8 ± 0.3

respectively. The FFT1 in Fig. 8b1 is obtained within the γ' region, which displays distinct superlattice reflections (highlighted by green circles), which is characteristic of the ordered $L1_2$ structure. In contrast, the FFT2 in Fig. 8b2 is obtained from the γ matrix shows the absence of such superlattice reflections. The lattice parameters a_γ, and $a_{\gamma'}$ estimated from the FFTs are 3.620 ± 0.068 Å, and 3.610 ± 0.026 Å, respectively and δ estimated using eq. (1) is −0.277 %. However, note that δ estimated from TEM are expected to overestimate the misfit of the bulk material [27]. This is because, the preparation of TEM samples involves thinning, which relaxes the native coherency stresses between the γ' precipitate and the matrix. Therefore, XRD analysis is performed on creep-tested samples to obtain δ for the bulk material, which are presented in **section S1** and listed in Table 3. The δ estimated from XRD is −0.191 %, which is lower than that obtained from FFT but significantly higher than that of undeformed AR sample. Fig. 8c shows the Dark Field (DF) TEM image of dislocations interacting with γ' precipitates. The alternate bright and dark bands observed within the γ' precipitates indicate that a pair of dislocations shears the γ' phase, as marked by white dashed circles in Fig. 8c. **Fig. S6** shows ~2 nm wide stacking faults within γ matrix.

Fig. 9a-c shows the TEM images of a creep-tested HT46 sample. In Fig. 9**a**, the STEM image reveals a uniform distribution of γ' precipitates within the γ matrix. The measured *d*, and λ of γ' precipitates, listed in Table 3, are 73 ± 13 nm and 101 ± 18 nm, respectively. Note that the γ' precipitate size in the HT46 sample prior to creep testing was only 20 ± 4 nm, suggesting that they coarsen during creep exposure to $t_r = 1413$ h. Moreover, δ of these γ' precipitates is −0.234 % (see Table 3 and section S1). Note that the δ has significantly increased compared to its undeformed counterpart, which is −0.058 %. Moreover, much like that observed in the creep-tested AR sample, several stacking faults are observed in the γ matrix of the creep-tested HT46 sample (see **Fig. S6b**), alternate dark and bright bands within the γ' precipitates are visible in the DF-TEM image (see Fig. 9**b**), and dislocation tangles are observed in the HAADF-STEM image (see Fig. 9**c**).

Similarly, the TEM images of the creep-tested HT470 sample are shown in Fig. 9d-f. The measured values of *d*, and λ of γ' precipitates are 90 ± 17 nm, 20 %, 124 ± 23 nm, respectively (see Table 3). Note that after creep while *d* has increased in size by ~2 times, λ has increased by ~2.5 times compared to that in the undeformed condition (see Table 2). δ of the creep-tested HT470 sample is −0.312 % (see Table 3 and section S1), which is ~5 times higher than that observed in its undeformed counterpart. Additionally, Fig. 9e-f and **Fig. S6c** reveal that the microstructural features on the creep-tested HT470 sample are similar to that in the creep-tested HT46 sample.

Finally, Fig. 9g-i shows the TEM images of the creep-tested HT6000 sample. The uniformly dispersed γ' precipitates have *d* and λ of 137 ± 27 nm and 189 ± 37 nm, respectively. Note that compared to that in the undeformed condition of the HT6000 sample, the γ' precipitates have only marginally coarsened and have an increased separation from 120 ± 27 nm and 165 ± 37 nm, respectively. The corresponding δ is −0.391 %, which is significantly higher than that in the undeformed HT6000 sample (see Table 2). Moreover, Fig. 9h-i show the HAADF-STEM images

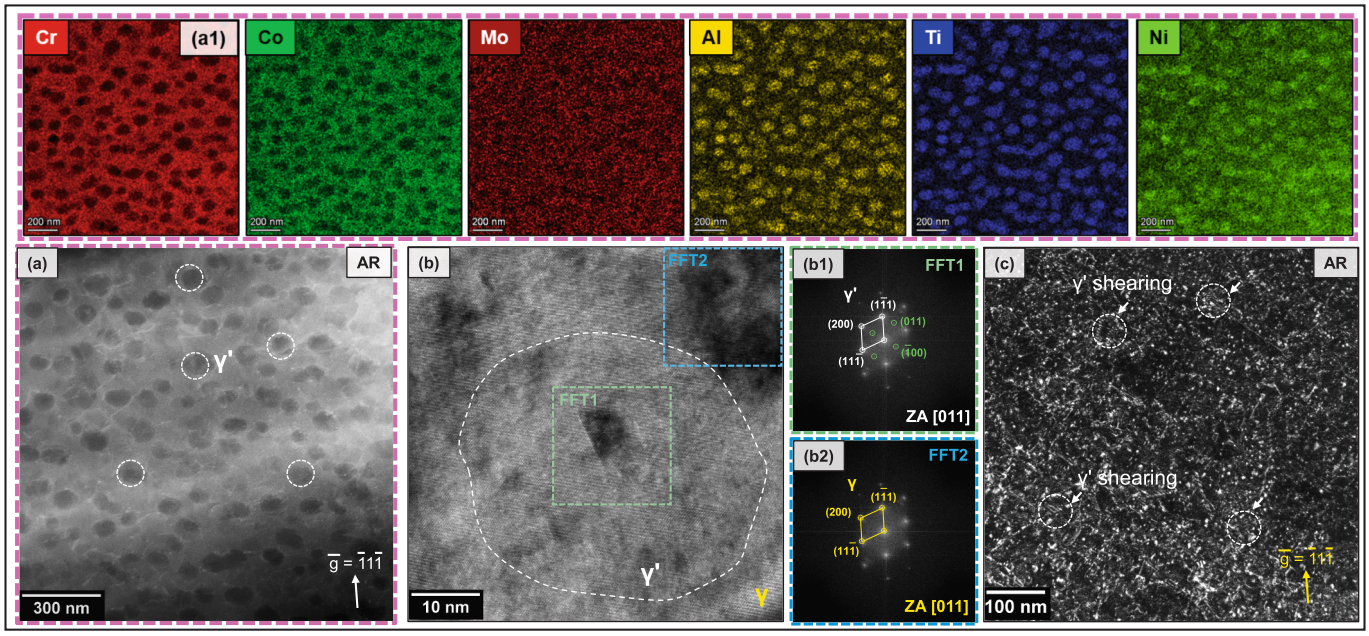


Fig. 8. Representative TEM micrographs of creep-tested AR samples tested at $T = 750$ °C and $\sigma_r = 300$ MPa (a) HAADF-STEM image of γ' precipitates and (a1) corresponding EDS elemental map. (b) Lattice fringes of γ matrix and γ' precipitates and corresponding FFTs of region delineated by (b1) green dashed line, (b2) blue dashed line, (c) DF-TEM image. (For interpretation of the references to colour in this figure legend, the reader is referred to the web version of this article.)

of the creep-tested HT6000 sample. Unlike that seen in AR, HT46 and HT470 samples, dislocation loops are observed around γ' precipitates and no alternate bands are observed within γ' precipitates. In addition, nanotwins are observed within the γ' precipitates, as highlighted by the yellow arrows. In addition to these, stacking faults are observed in γ matrix, which is similar to that observed in other creep tested samples (see **Fig. S6d**).

Overall, microstructural analysis of creep-tested AR and aged samples reveals that grain size remains largely invariant during creep exposure, while grain boundary carbide networks become denser and more continuous, with increased Mo-rich M_6C precipitation in aged samples. γ' precipitates evolve and coarsen during creep exposure along with increase in lattice misfit between γ and γ' phase. Creep deformation is dominated by dislocation-precipitate interactions, where alternate dark and bright bands within γ' precipitates are observed in AR, 46 h, and 470 h aged samples, whereas in 6000 h aged sample, dislocation loops around γ' precipitates are only observed.

3.4. Coarsening of γ' precipitates

During isothermal ageing of AR, γ' precipitates form and undergo coarsening, which manifests as the increase in d for samples aged at 46, 470 and 6000 h (HT46, HT470 and HT6000). Fig. 10 shows the variations of d with equivalent aging time (t_{ea}) in Haynes 282. For isothermally aged samples, t_{ea} corresponds to t_a. Also, d of all the samples, creep-tested at $T = 750$ °C and $\sigma_r = 300$ MPa, are included in the plot. To ensure equivalence with isothermal annealing data, t_{ea} of individual creep-tested samples is the sum of its t_a and t_r.

The data-points corresponding to d from isothermally annealed samples and creep-tested samples are represented by black and red solid circles, respectively. The classical Lifshitz-Slyozov-Wagner (LSW) theory [26] of precipitate coarsening is,

$$d^3 - d_o^3 = kt_{ea} \tag{5}$$

where d_o is the γ' precipitate size at $t_{ea} = 0$h. Note that eq. (5) fits all the data reasonably well, indicating that γ' coarsening during both creep and isothermal ageing are well-represented by the LSW precipitate coarsening model [28]. This indicates that precipitate coarsening is primarily sensitive to testing temperature and is broadly independent of the applied stress during creep.[1]

3.5. Fracture surface morphology

Fig. 11 displays the fracture surface morphology of creep-tested AR, HT46, HT470 and HT6000 samples tested at $T = 750$ °C and $\sigma_r = 300$ MPa. The SEM image of the creep-tested AR sample shows a rough, intergranular fracture surface with ductile dimples observed at higher magnification (see Fig. 11a and b). In addition, some creep cavities can be observed on the rough fracture surface, and within these cavities, fragments of second-phase particles are visible. This suggests that creep cavities form around second-phase particles, primarily around MC carbides (see **Figs. S7 and S8**). Similar fracture features are observed in HT46, HT470, and HT6000 creep-tested samples. In addition, creep cavities form at the interface between M_6C and primary MC carbides via interfacial decohesion (see **Figs. S7 and S8**).

4. Discussion

4.1. Microstructural evolution

Hot-rolled Haynes 282 forms coarse supersaturated equiaxed γ grains on solution treatment at 1050 °C. Note that γ' precipitates are absent in this condition as the treatment temperature is higher than the solvus temperature of γ' precipitates and grain boundary $M_{23}C_6$ carbides. Moreover, Haynes 282 has a low stacking fault energy, γ_{SF} of 27 mJ m^{-2} [12], which leads to the formation of annealing twins during strain relief [29]. This explains the presence of equiaxed γ grains with primary MC and a small fraction of M_6C carbides in the AR sample (see Fig. 1a and e).

[1] This inference is made for d measured from samples creep tested at 750 °C and 300 MPa and is therefore arguably representative of the other creep testing conditions where the temperature of testing is ±50 °C and applied stress is in the range 300–420 MPa. For other conditions, more systematic investigations are necessary.

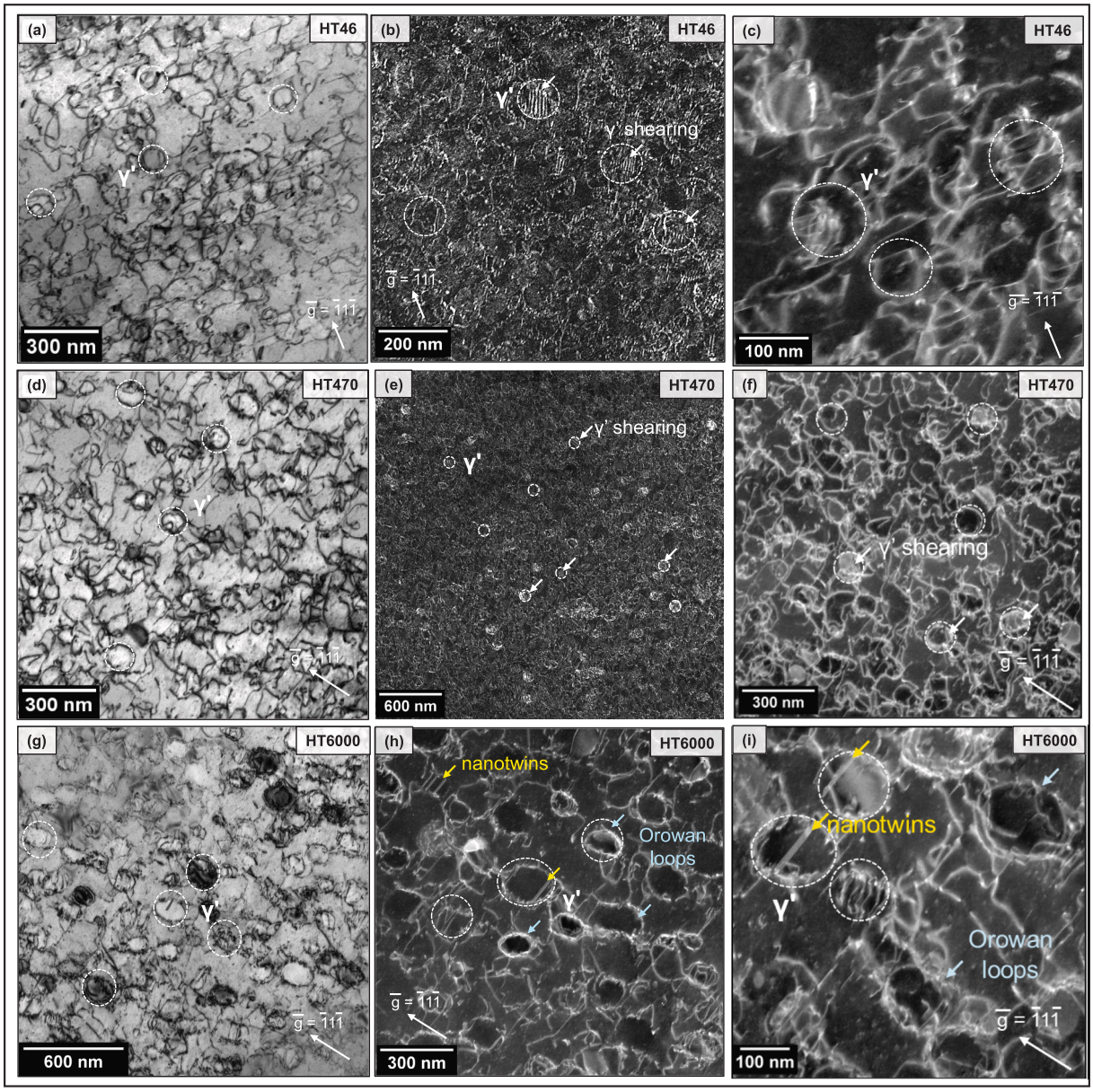


Fig. 9. Representative TEM micrographs of creep-tested HT46, HT470, and HT6000 samples tested at $T = 750$ °C and $\sigma_r = 300$ MPa. STEM image of γ' precipitates in (a) HT46, (d) HT470, and (g) HT6000 samples. DF-TEM and HAADF-STEM images of (b, c) HT46, (e, f) HT470 and (h, i) HT6000 samples.

On ageing, grain boundary carbides and γ' precipitates nucleate in the γ grains. Moreover, limited grain growth occurs even after long-term ageing due to the precipitation of $M_{23}C_6$ carbides along grain boundaries, which exerts Zener drag on them. The similar grain size of AR, HT46, HT470 and HT6000 samples is attributed to this effect (see Fig. 1i, j, k, l and Table 2). Simultaneously, ageing promotes γ' precipitation and subsequent coarsening via Ostwald ripening. Previous studies have shown that the γ' precipitates share the $\{100\}\gamma' || \{100\}\gamma$ and $\langle 100\rangle\gamma' || \langle 100\rangle\gamma$ orientation relationship with the γ matrix. Owing to this, when precipitates are fine, they are coherent with the matrix. On coarsening, the differences in the lattice parameters of γ and γ' leads to the development of interface strain, which leads to progressive loss of interface coherency. The progressive increase in δ of the γ'/γ interface with increasing ageing duration of aged Haynes 282 is attributed to this effect (see Table 2 and Fig. 2). In previous studies, it has been shown that γ'/γ interface becomes incoherent when the δ is >1 % [30–32]. However, amongst the aged samples in this work, the maximum measured δ of the γ'/ γ interface is only −0.174 %, which corresponds to that in the HT6000 sample (see Fig. 2). This implies that the γ'/ γ interfaces in all the aged samples, HT46, HT470 and HT6000, are coherent or semi-coherent. Additionally, prolonged ageing at 750 °C leads to segregation of Mo at the periphery of primary MC carbides, promoting their progressive degeneration and the formation of Mo-rich M_6C carbides at the MC/γ interface (see Fig. 1g). This MC → M_6C transformations, driven by refractory element redistribution, has been widely reported in Ni-based superalloys [33]. With further aging for 6000 h, M_6C carbides transform into needle-shaped TCP-μ phases (see Fig. 1h) [20].

4.2. Deformation mechanisms

In polycrystalline Ni-based superalloys, such as Haynes 282, the initial stage of creep deformation, in the temperature and stress range employed in this study, is characterized by dislocation multiplication and strong interactions between dislocations and γ′ precipitates [34,35]. The accumulation and interaction of dislocations progressively increase the internal resistance to deformation, resulting in strain hardening and

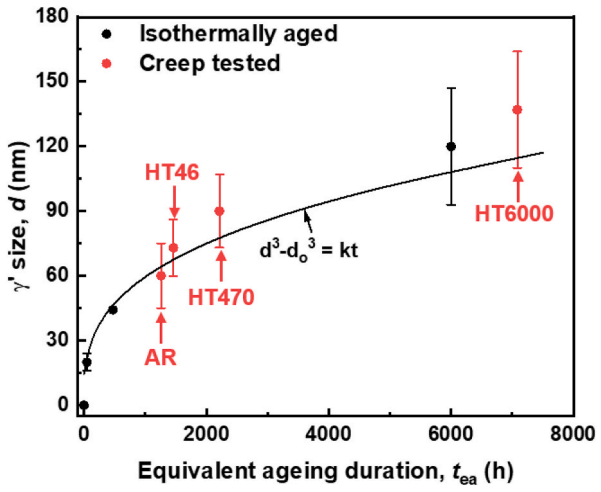


Fig. 10. Variation of γ' size as a function of equivalent ageing duration.

a reduction in the creep rate during primary creep. As the dislocation density increases, recovery processes, particularly dislocation climb, become increasingly relevant and progressively counteract the strain-hardening effect. Consequently, the primary creep regime becomes very short or difficult to distinguish. The absence of a primary creep regime in HT46 and HT470 samples is attributed to this effect (see **Table S1**). In HT6000 sample, the primary creep regime is present but comprises only ~1–5 % of the total creep life. The presence of this primary regime can be attributed to its higher λ compared to that in other samples. This is because higher λ allows dislocations a higher mean-free path before they are pinned by precipitates. Interestingly AR sample, which has no γ' precipitates initially also exhibits no primary creep strain. However, note that during creep testing, within 8 h, 15 nm fine precipitates nucleate in the matrix (see Fig. 10), which act as strong pinning points for dislocations. Consequently, primary creep regime is also absent in the AR sample. Therefore, creep in all the samples directly initiates in the steady state regime.

Additionally, the pinning of dislocations by the γ' precipitates requires additional stress for dislocation detachment to occur, which manifests as σ_{th}. Previous reports have shown that σ_{th} in Ni-based superalloys increases with increasing d [34]. This is attributed to the fact that for dislocations to detach from the γ' precipitates, it has to undergo glide across or climb over the γ' precipitates. Since the energy required to climb over or glide across larger precipitates is the product of the force on the dislocation and distance travelled, detachment from a precipitate with higher d, requires higher energy and hence higher σ_{th}. In addition, dislocation trapping is more pronounced at semi-coherent or incoherent γ and γ' interfaces than at coherent interfaces [35]. This is because, larger γ' precipitates have higher δ which helps in trapping dislocations more effectively. In addition, Kumar et al. [34], observed that selective segregation of Mo, Cr, and Co occurs near larger γ' precipitates compared to smaller ones, which exerts a stronger pinning force on the dislocation, which in turn also elevates σ_{th}. These effects explain the highest σ_{th} of HT6000, followed by that of HT470 and HT46 (see Fig. 5a).

After dislocation detachment, steady-state creep occurs, where the strain hardening is balanced by recovery processes. It is worth noting that a true steady state regime is only defined when the microstructure remains invariant. Therefore, since there is continuous microstructural evolution during creep testing of all the samples, a true steady state regime cannot be defined. Alternately, $\dot{\varepsilon}_{min}$, will be used as the appropriate parameter to nominally represent the steady-state creep deformation in all the following discussions. Creep recovery occurs via the dislocation climb-controlled creep mechanism, where dislocations undergo glide followed by climb to undergo mutual annihilation [36]. Note that since glide and climb are sequential processes, $\dot{\varepsilon}_{min}$ is influenced strongly by the rate of dislocation glide, which was also noted in our previous study on Inconel 740H [35]. In the context of glide rate, the balancing strain hardening mechanism during steady-state creep is the interaction of dislocations with γ' precipitates, which is summarized as follows. In the FCC-γ matrix, dislocations of the type $a_\gamma/2 < 111 >$ glide on {111} planes. However, owing to the moderately low γ_{SF} of Haynes 282, which is in the range of 20-40mJ m^{-2}, the dislocation dissociates into two $a_\gamma /6 < 112 >$ Shockley partials, which are separated by a stacking fault. The appearance of stacking faults in all creep-tested samples is attributed to this effect (see **Fig. S6**). If the γ' precipitate is coherent, it can be sheared by the partial dislocations. However, the strengthening from precipitate shearing depends on d and the width of the stacking fault, W_{sf} (or separation between partials). If d is similar to W_{sf}, shearing occurs via the 'weak pair-coupling' mechanism, where the leading partial individually shears the precipitate. This shearing by a partial dislocation leads to the formation of an anti-phase boundary (APB) that has higher energy than the stacking fault, owing to the disruption of chemical disordering in the γ' precipitate. The chemical order is restored, and APB is annihilated when the trailing partial subsequently shears the precipitate. If W_{sf} is large enough, such that the leading partial exits the precipitate and shears another precipitate before the trailing partial can exit the previously sheared precipitate, another APB forms. The formation of these multiple APB bands appears as alternate dark and bright contrast bands in DF-TEM images [37]. Such bands were indeed observed in the creep-tested AR and HT46 samples (see Figs. 8 and 9).

The stress for shearing γ' precipitate by the weak pair-coupling mechanism, τ_w, is [37],

$$\tau_w = \frac{\gamma_{APB}}{2b}\left[\left(\frac{6\gamma_{APB}fd}{\pi Gb^2}\right)^{\frac{1}{2}} - f\right] \tag{6}$$

where γ_{APB} is the antiphase boundary energy, which is 0.18 J m^{-2} for γ' in Haynes 282 [12], b is the Burgers vector of Shockley partials, which is 0.145 nm [38], f is the volume fraction of γ' precipitates, which is 20 % and G is the shear modulus of Haynes 282, which is 63 GPa at 750 °C [38]. The variations of τ_w as a function of d is shown in Fig. 12. Note that τ_w increases with increasing d. This is because, as d increases, the APB formed within the precipitates spans over a larger area. Since there is an energy penalty associated with increased APB energy, the motion of the leading partial is inhibited and a higher applied stress is required for further shearing, which in turn enhances τ_w. Previous studies have reported that the weak pair coupling mechanism is typically active d is in the range of 5–25 nm [37].

When d is significantly larger than W_{sf}, shearing occurs via the 'strong pair coupling' mechanism. In this case, the Shockley partials move in a coordinated manner and remain within the same precipitate during shearing. The corresponding shear stress for strong pair coupling [37], τ_s, is

$$\tau_s = \sqrt{\frac{3}{2}}\left(\frac{2Gb}{d}\right)f^{\frac{1}{2}}\frac{w}{\pi^{\frac{3}{2}}}\left(\left(\frac{\pi\gamma_{APB}d}{wGb^2}\right) - 1\right)^{\frac{1}{2}} \tag{7}$$

here, w accounts for the elastic interactions between partials, which is parameterized as a non-dimensional number equal to unity. Since the leading and trailing partials move together in a coordinated manner, the APB formed during shearing does not extend beyond their separation distance. Fig. 12 shows the variations of τ_s as a function of d. It can be observed that τ_s increases with increasing d. To understand this, note that the relationship between d and λ is [37],

$$\lambda = \frac{d}{2}\left(\frac{2\pi}{3f}\right)^{\frac{1}{2}} \tag{8}$$

Eq. (8) indicates that when d increases, λ also increases, which implies

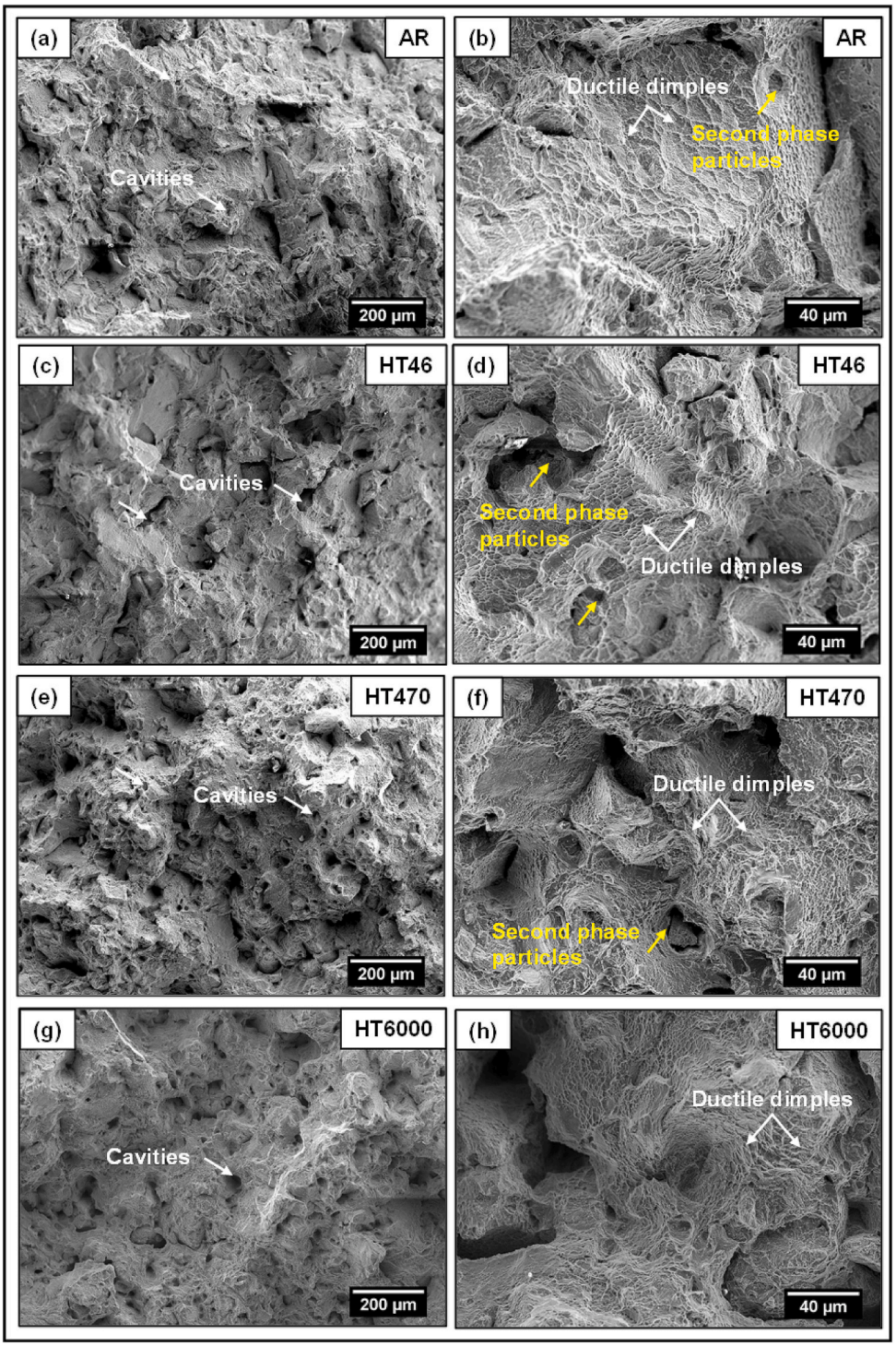


Fig. 11. Fracture surface morphology of creep-tested samples tested at $T = 750$ °C and $\sigma_r = 300$ MPa (a) and (b) AR samples, (c) and (d) HT46, (e) and (f) HT470, and (g) and (h) HT6000 samples.

that dislocations encounter fewer precipitates along their path, which reduces the frequency of shearing events. Consequently, the resistance to dislocation motion decreases, which in turn, explains the decrease in τ_s.

Typically, if the γ' precipitates are semi-coherent, shearing via the strong pair coupling mechanism is expected to be operational. In this study, d in the AR and HT46 samples increases from 0 nm to 60 ± 15 nm and 20 ± 4 nm to 73 ± 13 nm, respectively (see Fig. 10). This implies that dislocations initially cut precipitates in both samples via the weak pair coupling mechanism. However, after d exceeds 25 nm in both samples, the precipitates remain semi-coherent with the matrix as the δ of γ' precipitates in them is still <1 % for the entire duration of creep testing (see Table 3). Therefore, when d exceeds 25 nm in AR and HT46 samples, the shearing of precipitates occurs via the strong pair coupling mechanism. Similarly, d of the HT470 sample increases from 44 nm to 90 ± 17 nm during creep testing (see Table 2 and Table 3), which implies that even initially the precipitates are too coarse to undergo shearing via the weak coupling mechanism. However, for the entire duration of creep testing, δ of γ' precipitates remains below ~1 % (see Tables 3 and section S1), suggesting that the precipitate-matrix interface

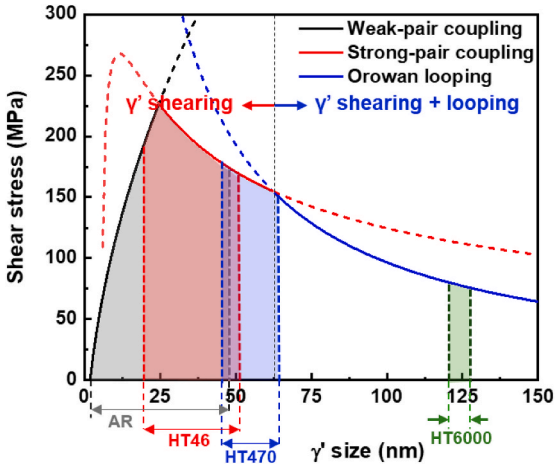


Fig. 12. Strength contribution from ordered γ' as a function of γ' particle size.

remains semi-coherent. This implies that while the dislocations will still shear the precipitates in the HT470 sample, only the strong coupling mechanism is active during its creep deformation. Similarly, the interface between γ' precipitates and the matrix in HT6000 is also semi-coherent over the entire duration of creep testing as its δ does not exceed 1 % (see Table 3). Therefore, since HT6000 has precipitates with d in the range of 120 ± 27–137 ± 27 nm during creep, the strong coupling mechanism is expected to be active in it. Interestingly, the γ' precipitates in the creep-tested HT6000 sample are largely unsheared and there is evidence that dislocations have rather bowed or bypassed them (see Fig. 9i). Moreover, the precipitates in the creep tested HT6000 sample contain nano-twins, which are otherwise absent in other creep tested samples (see Fig. 9i).

The formation of nanotwins during creep of Ni based superalloys has also been reported in some previous studies [39–41]. Knowles and Chen [42] noted that twins in γ' precipitates evolve from super intrinsic stacking faults (SISF) or super extrinsic stacking faults (SESF) when super partial dislocations operate over every adjacent plane or alternate plane in the γ' superlattice. However, they determined that a nanotwin nucleates in γ' precipitate only when it exceeds a critical size, d_c. Considering the change in free energy during the formation of a stacking fault (ΔE) within γ' precipitates depends on d, they derived the expression [42],

$$d_c = \frac{Gc^2b^2}{cb\tau - \gamma_{SF}} \tag{9}$$

Where c is the number of atomic layers in the nucleus, which is equal to 1[42] and τ is the resolved shear stress, which is 0.47 times the σ_r [42]. Using Eq. (9), d_c for Haynes 282 is 94 nm. Note that in all creep tested samples, except HT6000, $d < d_c$ (see Table 3). This explains the selective formation of twins within γ' precipitates in the HT6000 sample after creep testing. Additionally, we believe that the absence of precipitate shearing in HT6000 is an outcome of twin formation within γ' precipitates. Note that owing to the coherence of the γ'/γ interface in HT6000 samples, some dislocations from the γ matrix initially enter the γ' precipitates. However, once the stacking faults associated with these dislocations transform to twins, there is local lattice reorientation within the γ' precipitate. This lattice reorientation prevents continued slip of more dislocations across the sheared plane of the γ' precipitate. Consequently, to accommodate creep strain, dislocations bypass the precipitates via the Orowan looping mechanism, which explains the lack of precipitate shearing in the HT6000 sample. The stress required for dislocations to bypass γ' precipitates via Orowan looping, τ_o, is,

$$\tau_O = \frac{Gb}{\frac{d}{2}\left(\frac{2\pi}{3f}\right)^{\frac{1}{2}}} \tag{10}$$

The variations of τ_O as a function of d is shown in Fig. 12. Note that increase in d leads to a decrease in τ_O as there are wider channels available for dislocations to bow out and bypass the precipitates. It is important to note that τ_0 is strongly influenced by the γ′ volume fraction. For many single-crystal superalloys with a high γ′ volume fraction, the calculated τ_0 exceeds τ_s, thereby suppressing the transition from precipitate shearing to dislocation looping [43]. However, owing to its lower γ′ volume fraction, Haynes 282 exhibits a lower τ_0, allowing the shearing-to-looping transition to occur (see Fig. 12).

On the basis of the preceding discussions, the influence of ageing on dislocation glide resistance is summarized as follows. In Fig. 12, vertical dashed lines corresponding to the initial d and precipitate size at the end of steady-state creep stage, d_e, which is estimated from eq. (5) and Fig. 10 (see **Table S2**), in AR, HT46, HT470 and HT6000 samples, creep-tested at $T = 750$ °C and $\sigma_r = 300$ MPa are superimposed. Between these dashed lines, the operative strengthening mechanisms in each sample can be determined. In the AR and HT46 sample, the weak pair coupling mechanism is initially dominant, which means that the resistance to glide increases with creep duration. After d increases to 25 nm, the strong pair coupling mechanism is activated which leads to reducing glide resistance with increasing creep duration, which leads to the onset of tertiary creep. In the HT470 sample, only the strong pair coupling mechanism is active for the entire creep duration, which implies that the glide resistance continuously increases with increasing creep duration. In contrast, Orowan looping provides dislocation glide resistance in the HT6000 sample for the entire duration of creep. Note that the glide resistance due to Orowan looping is significantly lower than that provided by weak pair and strong pair coupling mechanisms, that are operative in other samples. The significantly higher $\dot{\varepsilon}_{min}$ of the HT6000 sample, compared to other samples, at $T = 750$ °C and $\sigma_r = 300$ MPa is attributed to this effect (see **Table S1**). Similarly, note that the glide resistance of HT470 sample is lower than that of HT46 over the entire duration of creep testing. However, this observation appears contradictory to the fact that HT470 sample has the lowest $\dot{\varepsilon}_{min}$ (see **Fig. S5** and **Table S1**). This discrepancy is resolved by considering that the rate of dislocation climb, which also instrumental in determining the overall $\dot{\varepsilon}_{min}$, is lower when d is higher. Note that dislocation climb involves diffusion of vacancies or atoms to the dislocation line so that it can escape the obstacle, which in this case, is the γ' precipitate. Consequently, dislocation climb rate is controlled by the diffusion rate of atoms and vacancies. Therefore, if d is larger, a larger number of atoms and vacancies need to diffuse to the dislocation for climb to occur, which in turn reduces the dislocation climb rate. Based on this argument, the dislocation climb rate in the HT470 sample, owing to its larger d, is expected to be considerably lower compared to that in HT46 sample. This decrease in the climb rate compensates for the higher rate of dislocation glide in the former and reduces its $\dot{\varepsilon}_{min}$, compared to that of the latter. By extension, it can also be argued that the climb rate in the HT6000 sample, which has the largest d, amongst all sample, is expected to be lowest, which in turn should lower its $\dot{\varepsilon}_{min}$. However, it appears that when d exceeds a certain limit, rate of dislocation glide becomes a more dominant factor in determining $\dot{\varepsilon}_{min}$. This is possibly due to the fact that precipitate coarsening widens the γ channels sufficiently to facilitate easier glide (see eq. (8)). Therefore, glide will have a greater contribution to creep strain compared to dislocation climb. This argument is further supported by the fact that Q_{app}, which is a strong descriptor of the underlying creep mechanism, of the HT6000 sample is significantly lower than that of HT46 and HT470. Consequently, we hypothesise that the slower rate of dislocation climb does not compensate for the higher rate of glide in the HT6000 sample, which results in its high $\dot{\varepsilon}_{min}$.

Although the above-mentioned analysis has been performed for a specific combination of T and σ_r, it is expected to be broadly valid for all the conditions considered in this work. This argument is supported by the fact that the LMP plots of all samples, except that of HT6000, have a single slope, which indicates that there is not a significant mechanism shift at any T and σ_r (see Fig. 6a). Also, the change in the slope of the LMP plot of the HT6000 sample at $\sigma_r \sim 390$ MPa could be related to the above-mentioned shift in the rate controlling step from climb to glide in the dislocation glide and climb controlled creep mechanism.

4.3. Creep failure and other considerations

Creep deformation in the tertiary regime is primarily governed by growth of voids and microcracks, as well as progressive microstructural instability [44,45]. These processes lead to strain localization that ultimately result in rupture. In general, while tertiary creep is characterized by crack initiation at the interface between carbides and the γ matrix followed by intergranual fracture (see **Fig. S7a, S7e, and S8a**), the failure mechanism depends on the thermal exposure of the alloy leading to rupture. In moderately aged alloys that are creep tested, MC carbides undergo some plastic deformation during creep. This was reported by Ge et al. [46] based on their observations of dislocations and shear offsets at the MC/γ interface. Furthermore, significant chromium segregation along these dislocations, combined with sustained dislocation climb, promotes the partial internal decomposition of MC carbides to $M_{23}C_6$. The resulting transformation leads to crack initiation at these locations [46]. The observation of fractured partially decomposed primary MC carbides in the BSE images of the AR and HT46 samples lends support to this mechanism. This is further confirmed by the presence of irregularly shaped cavities, of sizes comparable to those of primary MC carbides (see Fig. 11a and c) in AR and HT46 samples.

In more long-term aged samples, MC carbides decompose to M_6C carbides. These partially coherent M_6C/MC interfaces have high strain energy, which serve as preferential sites for crack nucleation and promote interfacial decohesion. These cracks eventually propagate along an increasingly dense and continuous network of grain boundary carbides leading to intergranular fracture. The observation of faceted surfaces in HT470 and HT6000 samples are attributed to this effect (Fig. 11e–f and g–h). Interestingly, while the HT6000 sample contains the hard and brittle TCP-μ phase, there is no evidence to support that it initiates creep fracture.

Before closing, it is important to discuss the implications of the results on current methodologies used for determining the long-term creep strength and rupture life of alloys. While the use of extrapolation methods is sometimes necessary, it is important to account for changes in the rate-controlling step within the creep mechanism to appropriately calibrate such extrapolations. In the present study, it is evident that just after being in service for 6 % of the total expected service life, there can be unexpected changes in the microstructure that can affect the creep behaviour of the alloy. One more interesting outcome of this study is that the growth of γ' precipitates is significantly more sensitive to thermal exposure compared to the applied stress (see Fig. 10). This enables damage accumulation or creep models that simulate overall creep behaviour or provide end-of-life projections to consider temperature and duration of service exposure as more critical parameters that dictate microstructural evolution.

5. Conclusion

The creep behavior of Haynes 282, in the solution-treated and three isothermally aged conditions, i.e., 750 °C for 46 h, 470 h, and 6000 h, is investigated temperature and stress range of 750–800 °C and 300–420 MPa. Some of the key conclusions of the study are as follows.

1. Isothermal ageing leads to progressive growth of γ' precipitates and the development of dense and continuous grain boundary carbide network with increasing ageing duration. The grain size changes marginally from 90 ± 8 to 163 ± 48 μm after 6000 h of ageing.
2. Creep tests reveal that the primary stage of creep is absent and the secondary and tertiary creep stages have similar spans. The minimum creep rate, $\dot{\varepsilon}_{min}$, decreases with ageing duration up to an ageing duration of 470 h but increases dramatically for the 6000 h aged sample. Larson-Miller Parameter plot and Monkman-Grant plot confirm that these trends are valid over the entire temperature and stress range of testing.
3. In the steady-state regime, artificially high values of n, were observed, indicating the presence of a threshold stress. The threshold stress increases with increasing ageing duration. On accounting for threshold stress, the effective stress exponent, n_{eff} is in the range of 4.7–5.9, which confirms that dislocation glide mediated climb is the rate-controlling mechanism during steady-state creep.
4. Post creep microstructural investigation reveals that γ' precipitates coarsen during creep. However, the precipitate coarsening kinetics during creep and isothermal annealing overlap, suggesting that the influence of stress is limited. γ' precipitates in all samples except the 6000 h aged sample appear to be sheared by dislocations and contain stacking faults. In contrast, the γ' precipitates in 6000 h aged sample contains nanotwins and are surrounded by dislocation networks.
5. Creep deformation is governed by the balance between glide/climb assisted recovery and strain hardening stemming from obstruction to the same. The glide resistance evolves from weak to strong pair coupling and ultimately to Orowan looping with increasing γ' size. Thus, γ′ coarsening does not alter the fundamental dislocation glide–climb controlled creep mechanism but changes the relative contribution and rate-controlling role of glide and climb, resulting in the observed variations in creep behavior.
6. Tertiary creep is governed by void nucleation, growth, and microstructural degradation, leading to accelerated deformation and rupture. In AR and 46 h aged samples, cracks initiate at MC carbide–γ interfaces due to elastic and thermal mismatch and propagate along grain boundary carbides, causing intergranular failure. In 470 and 6000 h aged samples, MC carbides transform to M_6C, creating high-energy interfaces that promote cavity formation and crack propagation along dense grain boundary networks.
7. Life assessment methods involving creep-life extrapolation must be performed with caution and with consideration of changes in the rate-controlling processes within the dislocation glide–climb controlled creep mechanism arising from continuous γ′ precipitate evolution.

CRediT authorship contribution statement

Amey Parnaik: Writing – original draft, Formal analysis, Data curation. **Vijay Shankar Sridharan:** Visualization. **Kai Chen:** Validation. **G.A. Turichin:** Resources. **O.G. Klimova-Korsmik:** Resources. **A. H.V. Pavan:** Methodology, Investigation, Conceptualization. **R.L. Narayan:** Writing – review & editing, Writing – original draft, Supervision, Project administration, Funding acquisition.

Declaration of competing interest

The authors declare that they have no known competing financial interests or personal relationships that could have appeared to influence the work reported in this paper.

Acknowledgements

Thank you, Prof. K C Harikumar, MME, IITM, for the Thermocalc support. The authors gratefully acknowledge the Prime Minister Research Fellowship (PMRF) for financially supporting this research, the Central Research Facility (CRF), IIT Delhi, for providing essential research facilities, and the valuable assistance of Mr. Kishor Kaushal

Kumar in sample preparation. This work was partially funded by the Russian Science Foundation Grant no. 25-79-30012 (https://rscf.ru/en/project/25-79-30012/) and ARDB, DRDO (project number: ARDB/MM/4144/400/R&D/2025/2176). RLN wants to thank Mr. Shubham Tiwari for the best finance manager the world has ever seen. This research is because of the time he buys with his phenomenal work.

Appendix A. Supplementary data

Supplementary data to this article can be found online at https://doi.org/10.1016/j.matdes.2026.117112.

Data availability

Data will be made available on request.

References

[1] L.M. Pike, HAYNES® 282™ alloy: a new wrought superalloy designed for improved creep strength and fabricability, in: Proceedings of the ASME Turbo Expo 4, 2008, pp. 1031–1039, https://doi.org/10.1115/GT2006-91204.
[2] K.L. Kruger, HAYNES 282 alloy, in: Materials for Ultra-Supercritical and Advanced Ultra-Supercritical Power Plants, 2017, pp. 511–545, 10.1016/B978-0-08-100552-1.00015-4.
[3] A. Muhammad, N. Park, Haynes 282 Superalloy: Advancements, challenges, applications, and future perspectives, in: Transactions of the Indian Institute of Metals, 2025, pp. 1–18, 10.1007/S12666-025-03678-9.
[4] A.H.V. Pavan, R.L. Narayan, S.H. Li, K. Singh, U. Ramamurty, Mechanical behavior and dynamic strain ageing in Haynes®282 superalloy subjected to accelerated ageing, Mater. Sci. Eng. A 832 (2022) 142486, https://doi.org/10.1016/J.MSEA.2021.142486.
[5] P.F. Tortorelli, H. Wang, K.A. Unocic, M.L. Santella, J.P. Shingledecker, V. Cedro, Long-term creep-rupture behavior of Inconel® 740 and Haynes® 282, in: ASME 2014 Symposium on Elevated Temperature Application of Materials for Fossil, Nuclear, and Petrochemical Industries, ETAM 2014, 2017, pp. 29–36, 10.1115/ETAM2014-1003.
[6] M.L. Santella, P.F. Tortorelli, M. Render, B. Pint, H. Wang, V. Cedro, X. (Frank) Chen, Effects of applied stress and grain size on creep-rupture lifetime prediction for Haynes 282 alloy, Mater. Sci. Eng.: A 838 (2022) 142785, https://doi.org/10.1016/J.MSEA.2022.142785.
[7] H. Liu, X. Zhao, Q. Yue, Y. Gu, Microstructure and deformation mechanism of Ni-based wrought superalloys for A-USC power plants: a review, J. Mater. Sci. 11 (59) (2024) 4404–4430, https://doi.org/10.1007/S10853-024-09517-4.
[8] C.J. Boehlert, S.C. Longanbach, A comparison of the microstructure and creep behavior of cold rolled HAYNES® 230 alloy™ and HAYNES® 282 alloy™, Mater. Sci. Eng. A 528 (2011) 4888–4898, https://doi.org/10.1016/J.MSEA.2011.03.019.
[9] M. Tamura, F. Abe, K. Shiba, H. Sakasegawa, H. Tanigawa, Larson-miller constant of heat-resistant steel, Metall. Mater. Trans. a Phys. Metall. Mater. Sci. 44 (2013) 2645–2661, https://doi.org/10.1007/S11661-013-1631-0/FIGURES/22.
[10] S. Mukherjee, S. Kumar Kar, S. Sivaprasad, S. Tarafder, G.B. Viswanathan, H. L. Fraser, Creep-fatigue response, failure mode and deformation mechanism of HAYNES 282 Ni based superalloy: effect of dwell position and time, Int. J. Fatigue 159 (2022) 106820, https://doi.org/10.1016/J.IJFATIGUE.2022.106820.
[11] L. Wang, K. Mao, P.F. Tortorelli, P.J. Maziasz, M. Thangirala, K.A. Unocic, X. F. Chen, Effect of heterogeneous microstructure on the tensile and creep performances of cast Haynes 282 alloy, Mater. Sci. Eng. A 828 (2021) 142099, https://doi.org/10.1016/J.MSEA.2021.142099.
[12] A.H.V. Pavan, A. Parnaik, S.H. Li, U. Ramamurty, R.L. Narayan, Effect of long-term ageing and associated precipitation on the fatigue crack growth behaviour of a ni-based superalloy, Metall. Mater. Trans. A 57 (3) (2026) 1321–1338, https://doi.org/10.1007/s11661-026-08138-7.
[13] A. Parnaik, A.H.V. Pavan, S.S. Silchonok, N.G. Kislov, R.L. Narayan, High-cycle fatigue behavior of Haynes 282 superalloy subjected to accelerated ageing, Int. J. Fatigue 182 (2024) 108234, https://doi.org/10.1016/J.IJFATIGUE.2024.108234.
[14] S. Mukherjee, K. Barat, S. Sivaprasad, S. Tarafder, S.K. Kar, Elevated temperature low cycle fatigue behaviour of Haynes 282 and its correlation with microstructure – effect of ageing conditions, Mater. Sci. Eng. A 762 (2019) 138073, https://doi.org/10.1016/J.MSEA.2019.138073.
[15] S. Mukherjee, B.P. Sahu, S.K. Sarkar, S. Ahlawat, A. Biswas, G.K. Mandal, S. Tarafder, S.K. Kar, Temporal evolution of γ′ precipitate in HAYNES 282 during ageing: growth and coarsening kinetics, solute partitioning and lattice misfit, Materialia (Oxf). 26 (2022) 101633, https://doi.org/10.1016/J.MTLA.2022.101633.
[16] HAYNES ® 282 ® alloy Principal Features, Haynes® International High Temperature Alloys - Haynes® 282® Alloy (2019) (2023). http://haynesintl.com/docs/default-source/pdfs/new-alloy-brochures/high-temperature-alloys/brochures/282-brochure.pdf (accessed May 30, 2026).
[17] ASTM E8/E8M-13a, Standard Test Methods for Tension Testing of Metallic Materials, ASTM International, West Conshohocken, PA, 2013, 10.1520/E0008_E0008M-22.
[18] ASTM E139-11(2018) Test Methods for Conducting Creep, Creep-Rupture, and Stress-Rupture Tests of Metallic Materials, ASTM International, West Conshohocken, PA (2013), (2018). https://doi.org/10.1520/E0139-11R18.
[19] R. Buerstmayr, B. Schulz, E. Povoden-Karadeniz, E. Kozeschnik, M. Lison-Pick, S. Primig, Improved thermodynamic descriptions of carbides in Ni-based superalloys, JOM 76 (5) (2024) 2283–2301, https://doi.org/10.1007/S11837-024-06484-8.
[20] Z. Zhang, Z. Yue, TCP phases growth and crack initiation and propagation in nickel-based single crystal superalloys containing Re, J. Alloys Compd. 746 (2018) 84–92, https://doi.org/10.1016/J.JALLCOM.2018.02.133.
[21] H. Mughrabi, The importance of sign and magnitude of γ/γ′ lattice misfit in superalloys—with special reference to the new γ′-hardened cobalt-base superalloys, Acta Mater. 81 (2014) 21–29, https://doi.org/10.1016/j.actamat.2014.08.005.
[22] R.W. Schirmer, S. Roth, M. Abendroth, B. Kiefer, An advanced creep law for large stress and temperature ranges, derived from the Larson-Miller master curve concept, Int. J. Press. Vessel. Pip. 218 (2025) 105585, https://doi.org/10.1016/J.IJPVP.2025.105585.
[23] E.W. De Reca, C. Pampillo, Self-diffusion of Ni in Ni-Fe alloys, Acta Metall. 15 (1967) 1263–1268, https://doi.org/10.1016/0001-6160(67)90001-6.
[24] X. Wu, R. Liu, X. Wu, S. Li, F. Khelfaoui, Assessment of creep properties of haynes 282 weld using deformation mechanism-based true stress model, J. Mater. Eng. Perform. 34 (15) (2024) 16273–16283, https://doi.org/10.1007/S11665-024-10281-4.
[25] G. Sundararajan, The Monkman-grant relationship, Mater. Sci. Eng. A 112 (1989) 205–214, https://doi.org/10.1016/0921-5093(89)90360-2.
[26] J.A. Hawk, T. Le Cheng, J.S. Sears, P.D. Jablonski, Y.H. Wen, Gamma prime stability in haynes 282: theoretical and experimental considerations, J. Mater. Eng. Perform. 24 (2015) 4171–4181, https://doi.org/10.1007/S11665-015-1711-Y/FIGURES/9.
[27] C. Schulze, M. Feller-Kniepmeier, Transmisson electron microscopy of phase composition and lattice misfit in the Re-containing nickel-base superalloy CMSX-10, Mater. Sci. Eng. A 281 (2000) 204–212, https://doi.org/10.1016/S0921-5093(99)00713-3.
[28] N. Boonlert, Z. Wang, K. Chen, H. Shen, P. Zhang, R.L. Narayan, Cooling rate and solution temperature dependent γ' coarsening mechanism in DZ125 Ni-based superalloy, Mater Charact 228 (2025) 115429, https://doi.org/10.1016/J.MATCHAR.2025.115429.
[29] S.K. Pradhan, S. Mandal, C.N. Athreya, K.A. Babu, B. de Boer, V.S. Sarma, Influence of processing parameters on dynamic recrystallization and the associated annealing twin boundary evolution in a nickel base superalloy, Mater. Sci. Eng. A 700 (2017) 49–58, https://doi.org/10.1016/J.MSEA.2017.05.109.
[30] H. Long, H. Wei, Y. Liu, S. Mao, J. Zhang, S. Xiang, Y. Chen, W. Gui, Q. Li, Z. Zhang, X. Han, Effect of lattice misfit on the evolution of the dislocation structure in Ni-based single crystal superalloys during thermal exposure, Acta Mater. 120 (2016) 95–107, https://doi.org/10.1016/J.ACTAMAT.2016.08.035.
[31] L. Dirand, J. Cormier, A. Jacques, J.P. Chateau-Cornu, T. Schenk, O. Ferry, P. Bastie, Measurement of the effective γ/γ′ lattice mismatch during high temperature creep of Ni-based single crystal superalloy, Mater Charact 77 (2013) 32–46, https://doi.org/10.1016/J.MATCHAR.2012.12.003.
[32] D.M. Collins, L. Yan, E.A. Marquis, L.D. Connor, J.J. Ciardiello, A.D. Evans, H. J. Stone, Lattice misfit during ageing of a polycrystalline nickel-base superalloy, Acta Mater. 61 (2013) 7791–7804, https://doi.org/10.1016/J.ACTAMAT.2013.09.018.
[33] Y. Yang, Y. Gao, C. Liu, J. Dong, L. Lou, Synergistic evolution of MC/M23C6 carbides in a polycrystalline Ni-based superalloy during long-term aging: Elemental diffusion and interaction mechanisms, Mater Charact 229 (2025) 115462, https://doi.org/10.1016/J.MATCHAR.2025.115462.
[34] C. Kumar, A.H.V. Pavan, S.K. Makineni, P. Kumar, Role of threshold stress in creep of IN740H, a γ′-lean Ni-based superalloy, Mater. Sci. Eng. A 903 (2024) 146667, https://doi.org/10.1016/j.msea.2024.146667.
[35] A. Parnaik, A.H.V. Pavan, S.H. Li, U. Ramamurty, R.L. Narayan, Effect of γ′ size on the Stress-Rupture Behaviour of Inconel 740H Superalloy, Adv. Eng. Mater. (2026) e202503206, https://doi.org/10.1002/ADEM.202503206; SUBPAGE:STRING:FULL.
[36] J. Weertman, Theory of steady-state creep based on dislocation climb, J. Appl. Phys. 26 (1955) 1213–1217, https://doi.org/10.1063/1.1721875.
[37] R.C. Reed, The Superalloys: Fundamentals and Applications, Cambridge University Press, 2008.
[38] P. Zhang, Y. Yuan, H. Yin, Y. Gu, J. Wang, M. Yang, G. Yang, X. Song, Tensile properties and deformation mechanisms of haynes 282 at various temperatures, Metall. Mater. Trans. A 49 (5) (2018) 1571–1578, https://doi.org/10.1007/S11661-018-4515-5.
[39] G.B. Viswanathan, S. Karthikeyan, P.M. Sarosi, R.R. Unocic, M.J. Mills, S. Karthikeyanz, P.M. Sarosiy, R.R. Unocicy, M.J. Millsy, Microtwinning during intermediate temperature creep of polycrystalline Ni-based superalloys: mechanisms and modelling, Phil. Mag. 86 (2006) 4823–4840, https://doi.org/10.1080/14786430600767750.
[40] M.G. Ardakani, M. McLean, B.A. Shollock, Twin formation during creep in single crystals of nickel-based superalloys, Acta Mater. 47 (1999) 2593–2602, https://doi.org/10.1016/S1359-6454(99)00145-7.
[41] R.R. Unocic, G.B. Viswanathan, P.M. Sarosi, S. Karthikeyan, J. Li, M.J. Mills, Mechanisms of creep deformation in polycrystalline Ni-base disk superalloys, Mater. Sci. Eng. A 483–484 (2008) 25–32, https://doi.org/10.1016/J.MSEA.2006.08.148.

[42] D.M. Knowles, Q.Z. Chen, Superlattice stacking fault formation and twinning during creep in γ/γ′ single crystal superalloy CMSX-4, Mater. Sci. Eng. A 340 (2003) 88–102, https://doi.org/10.1016/S0921-5093(02)00172-7.
[43] Y. Zhao, Z. Wang, L. Shi, S. Gao, D. Qian, K. Chen, Y. Li, W. Pantleon, Simultaneous strength optimization and recrystallization prevention in induction-heating-assisted laser additively manufactured Ni-based superalloys, Mater. Res. Lett. 13 (2025) 632–641, https://doi.org/10.1080/21663831.2025.2491566.
[44] A. Staroselsky, B. Cassenti, Mechanisms for tertiary creep of single crystal superalloy, Mech. Time-Depend. Mater. 12 (4) (2008) 275–289, https://doi.org/10.1007/S11043-008-9065-6.
[45] B.F. Dyson, T.B. Gibbons, Tertiary creep in nickel-base superalloys: analysis of experimental data and theoretical synthesis, Acta Metall. 35 (1987) 2355–2369, https://doi.org/10.1016/0001-6160(87)90083-6.
[46] H. Ge, G. Liu, S. Zheng, Y. Yang, K. Liu, X. Ma, Dislocation climbing dominated decomposition and fracture of carbides in a Ni-based superalloy, Acta Mater. 246 (2023) 118669, https://doi.org/10.1016/J.ACTAMAT.2023.118669.